Computer Modeling in Engineering & Sciences

Tech Science Press

https://doi.org/10.32604/cmes.2026.079635

ARTICLE

Second-Law Analysis of Double Diffusive Convection of Casson Ternary Nanofluid in a Porous Enclosure with a T-Shaped Baffle

Sarna Soren[1], Samrat Hansda[1,*], Umair Khan[2,3], Anuar Ishak[4], Ahmed Kadhim Hussein[5] and Md Mamun Molla[6,7]

[1]Department of Mathematics, Sidho-Kanho-Birsha University, Purulia, West Bengal, India
[2]Department of Mathematics, School of Engineering, Saveetha Institute of Medical and Technical Sciences, Saveetha University, Chennai, Tamil Nadu, India
[3]Department of Mathematics, Faculty of Science, Sakarya University, Serdivan/Sakarya, Turkey
[4]Department of Mathematical Sciences, Faculty of Science and Technology, Universiti Kebangsaan Malaysia (UKM), Bangi, Selangor, Malaysia
[5]Department of Mechanical Engineering, University of Babylon, Hilla, Iraq
[6]Department of Mathematics & Physics, North South University, Dhaka, Bangladesh
[7]Center for Applied and Computational Science (CACS), North South University, Dhaka, Bangladesh

*Corresponding Author: Samrat Hansda. Email: samrathansda143@gmail.com

Received: 25 January 2026; Accepted: 18 March 2026; Published: 27 May 2026

ABSTRACT: This study presents a numerical investigation of thermosolutal convection within a baffled porous cavity filled with a radiative Casson-based ternary aqueous nanofluid. The ternary hybrid nanofluid is formulated by dispersing three distinct nanoparticles into a water-based solution, aiming to enhance the thermal and solute transport characteristics. The cavity includes internal baffles that modulate convective flow and facilitate improved energy transport. The governing equations for momentum, energy, species concentration, and entropy generation are discretized and solved using a higher-order compact (HOC) finite difference scheme, ensuring superior numerical precision. The novelty of the present study lies in the irreversibility analysis of thermosolutal convection of a Casson ternary nanofluid in a porous wavy enclosure with a T-shaped baffle, highlighting the combined effects of non-Newtonian behavior, ternary nanoparticle interaction, and geometric modification on entropy generation and transport performance. The impacts of key physical parameters on solutal and thermal distributions, entropy generation, and the Bejan number are systematically examined. The study reveals that the combined influence of the non-Newtonian nature of the Casson fluid and thermal radiation significantly alters flow structure and transport rates. Enhanced heat transfer is observed with increasing radiation parameters, while solutal transport remains relatively less sensitive. The presence of internal baffles promotes localized vortices and thermal layering, contributing to complex thermo-solutal interactions. The outcomes also show that the inclusion of a T-shaped baffle within the container enhances overall convective transport characteristics and system performance. The findings provide valuable insights into the design of advanced energy systems involving non-Newtonian nanofluids in porous enclosures under radiative and geometric constraints.

KEYWORDS: Thermosolutal convection; T-shaped baffle; Casson fluid; ternary hybrid nanofluid; entropy generation; thermal radiation; wavy enclosure

1 Introduction

In recent years, baffled enclosures have gained considerable attention in thermal management applications such as air conditioners, refrigerators, cooling fans, double-pipe, and air-cooled heat exchangers [1,2].

A growing area of interest within such systems is double-diffusive convection (DDC), where both temperature and concentration gradients drive fluid motion. In an H-shaped container with corrugated walls and a baffle, Eshaghi et al. [3] evaluated DDC and revealed that when increasing in buoyancy ratio, both the heat and mass transfer increased. In a curvy porous chamber of U-shaped with an inverse T-shaped baffle inside, Hansda et al. [4] exposed the analysis of radiative nanofluid magneto-thermogravitational convection. They noticed that the Bejan number and Nusselt number upgraded when the nanoparticle volume fraction (ϕ_{hnf}) improved, but the total entropy generation is inversely proportional to ϕ_{hnf}. In a wavy baffled porous geometry, Hansda et al. [5] evaluated the performance of the hydromagnetic and thermosolutal radiative hybrid nanofluid. They observed that as the Rayleigh number (Ra) improves from 10^4 to 10^6, both the heat and the mass transfer improve. Kouki et al. [6] analyzed thermosolutal buoyancy-driven flow of a suspension containing nano-encapsulated phase change materials. The investigation employed the finite element method in combination with an ANN-based multilayer perceptron (MLP) algorithm to predict transport behavior and optimize system performance. They found that as Ra increases, the phase change area grows. In a recent study, Alsedais and Aly [7] investigated DDC induced by an oscillating fin embedded within an asteroid-shaped cavity filled with nano-encapsulated phase change materials. Using the ISPH (Incompressible Smoothed Particle Hydrodynamics) method, they analyzed the coupled heat and mass transfer behavior and highlighted the significant influence of baffle oscillation and complex geometry on flow structure and thermal performance. Their findings provide valuable insight into the enhancement of convective transport in irregular enclosures containing advanced thermal storage materials. Ahmad et al. [8] numerically investigated DDC in a cavity with non-uniformly heated walls. The results demonstrated that both the Hartmann number and a wall heating configuration significantly influence the convective intensity and thermal performance inside the enclosure.

In the current era, growing interest has emerged in exploring irregular geometries with DDC, specifically wavy-walled cavities, because of their potential in improving thermal and solute transport via surface modulation. Unlike traditional rectangular domains, wavy enclosures bring out the transformation in concentration and temperature through the surface. These transformations help the fluid mix better, move faster, and impact how stable the flow is. Also, these geometries are particularly applicable in engineering systems where enhanced thermal behavior and desired mixing efficiency are needed. Inside a two-wavy-walled cavity, Jain et al. [9] examined the simulation of DDC using a power-law nanofluid. In the results, the rate of thermal and solute transport increased with increasing numbers of Ra. Hansda et al. [10] investigated the study of magnetically impacted DDC of radiative hybrid nanofluid in a porous chamber with wavy walls with nonuniform heating and stated that the average Nusselt number and the average Sherwood number increased by increasing the Rayleigh number and Darcy number. Parmar et al. [11] evaluated a study on DDC in a porous wavy-walled chamber with time-frictional impacts. They found that fractional parameter solute and heat transport greatly impact the early performance of temperature lines, streamlines, and concentration lines. Parmar et al. [12] investigated the algorithmic study of DDC in a nanofluid within a wavy-walled porous geometry using fractional order. Alomari et al. [13] presented a study of DDC in three fins inside a wavy geometry used by nanofluid. They noted that as nanoparticle volume fraction (ϕ), Rayleigh number (Ra), and heat source/sink (q) improve, thermal and solute transport are enhanced. In a non-uniform porous chamber, Chuhan et al. [14] exposed thermosolutal convection affected by an inclined magnetic field. Hansda et al. [15] analyzed irreversibility during double diffusion in a wavy porous geometry filled with a radiative hybrid ferrofluid, while in related work, they reported enhanced DDC performance using radiative ternary hybrid nanofluids compared to hybrid and mono nanofluids. In a baffled inside porous, curvy H-shaped chamber with nanoencapsulated PCMs and the influence of heat parameters, Irshad et al. [16] studied DDC and found that the buoyancy ratio (N) and the Rayleigh number (Ra) have a positive impact on convective

species and energy transport. Tayebi et al. [17] evaluated energy management and DDC in a novel wavy I-shaped enclosure with nano-PCM, affected by Soret and Dufour. The entropy generation of thermal and solute transport increases as the flow becomes slow. In a wavy square geometry, Uddin et al. [18] examined the influence of hydromagnetic fields on the DDC of a Cu-H_2O nanofluid. Investigations addressing DDC in wavy geometries are also available in [19–22]. However, the aforementioned studies did not address the influence of Casson fluid on DDC.

Despite their real-world relevance, particularly in biomedical and industrial applications, DDC in Casson fluids, especially within porous cavities, remains underexplored [23–26]. The majority of available studies emphasize Newtonian or conventional non-Newtonian fluids, while the distinctive yield stress and viscosity behavior of Casson fluids remains underexplored. This work addresses that gap by analyzing how these properties influence thermal and solute transport in a bounded domain, advancing thermal-fluid modeling for complex systems. Casson fluids, unlike Newtonian fluids, behave as solids until a yield stress is exceeded, after which they flow like viscous fluids. Examples include blood, toothpaste, paint, and chocolate. The Casson model finds widespread use in biological and industrial processes, where previous studies have examined its behavior in porous media and confined flows, emphasizing its role in thermal and solute transport. In this context, Alomari et al. [27] investigate double-diffusive transport and entropy generation of a Casson $Cu - H_2O$ nanofluid in a wavy cylindrical chamber with an inner heated core, including MHD and thermal radiation effects, and report how parameters such as Ra, Ha, the Casson parameter, radiation, and buoyancy ratio affect heat transfer and irreversibility in that geometry. Salho et al. [28] studied the entropy generation and thermo-fluid dynamics of $Cu - H_2O$ Casson fluid in an H-shaped cavity with corrugated cylinders, focusing on MHD, radiation, and transport effects over a wide parametric range, and provided insights relevant to enclosure design for thermal management. In a wavy-shaped geometry, Hussain et al. [29] studied the effect of MHD and irreversibility of non-Newtonian fluids (Casson fluids) on DDC. They noticed how rising Le from 0.1 to 10 decreased the total entropy generation. In square geometry, Aghighi et al. [30] evaluated the Casson fluid moving in the DDC. In a wavy top chamber, Rashid et al. [31] employed heat transport examinations of the flow under a magnetic field with DDC in a Casson material. Upon improvement of the Ha values, the heat and mass flux decreased. Within a hexagonal geometry, Shah et al. [32] performed the magnetically affected Casson fluid flow in the DDC. In a wavy geometry used by the Casson fluid, Chuhan et al. [33] evaluated the reduction of the magnetic field entropy of DDC. In a square porous geometry containing Casson fluid, Aneja and Sharma [34] researched energy and species transport due to DDC. Chuhan et al. [35] performed an angled magnetic field impact on DDC under a curvy cavity used by Casson fluid. The heat flux improves when the non-Newtonian parameters are increased, which was noticed by them. In a curvy geometry used by the Casson fluid and baffle, Hansda et al. [36] looked into the thermosolutal behavior of entropy generation and different heating approaches. They noticed that the Casson fluid parameter (γ) could enhance the kinetic energy, energy, and solutal transfer. Kathyayani and Venkata Ramudu [37] examined the magnetic field in the DDC of chemical reactions and thermal radiation in a triangular geometry filled with Casson fluid.

Despite significant progress in the study of double-diffusive convection (DDC) in wavy and irregular geometries, limited attention has been devoted to thermosolutal convection involving ternary hybrid nanofluids in baffled porous enclosures, particularly when coupled with non-Newtonian rheology and second-law analysis. In many practical applications—such as solar-assisted cavities, electronic cooling modules, compact heat exchangers, and thermal energy storage systems—non-uniform heating and internal obstructions (e.g., T-shaped baffles) are unavoidable and substantially influence heat and mass transport characteristics. Moreover, dispersing multiple nanoparticles into a non-Newtonian base fluid like a Casson fluid introduces additional complexity due to yield-stress behavior, viscosity variation, and enhanced

effective thermal conductivity. The combined influence of these factors on thermodynamic irreversibility remains largely unexplored. To address these gaps, this work numerically examines thermosolutal convection and entropy generation in a porous wavy enclosure filled with a Casson-based ternary hybrid nanofluid in the presence of a centrally mounted T-shaped baffle. The ternary nanofluid utilized in this study combines magnetic oxide (Fe_3O_4), thermally and electrically conductive multi-walled carbon nanotubes (MWCNTs), and highly conductive Copper (Cu) nanoparticles, offering a unique blend of properties that enhance stability, heat transfer efficiency, and thermal conductivity. Such nanofluids are particularly suitable for applications in advanced heat exchangers, electronic cooling devices, solar thermal systems, nuclear cooling technologies, and magnetically assisted thermal management processes. The novelty of this work lies in the unified integration of Casson rheology, ternary nanoparticle suspension, thermosolutal buoyancy coupling, porous medium resistance, geometric waviness, and internal baffling within a comprehensive second-law framework. The coupled effects of the governing parameters on flow behavior, heat and mass transfer, entropy generation, and Bejan number are systematically examined to identify thermodynamically optimal conditions. The objective of the present study is to numerically investigate thermosolutal convection and entropy production in a porous wavy enclosure filled with a Casson-based trihybrid nanofluid in the presence of a centrally mounted T-shaped baffle. The study aims to elucidate the coupled effects of non-Newtonian Casson rheology, ternary nanoparticle dispersion, porous medium resistance, and thermosolutal buoyancy on flow behavior, heat and mass transfer, and thermodynamic irreversibility. Emphasis is placed on second-law analysis through the evaluation of entropy generation and Bejan number to identify optimal conditions that balance transport enhancement and irreversibility minimization, thereby providing useful design guidelines for high-efficiency thermal systems operating in geometrically complex porous enclosures. By simultaneously evaluating transport enhancement and irreversibility minimization, this study provides new physical insights and practical design guidelines for high-efficiency thermal management systems employing advanced non-Newtonian ternary nanofluids in geometrically complex porous domains.

2 The Problem and Governing Equations

The schematic diagram of this investigation is a two-dimensional wavy enclosure, as displayed in Fig. 1. The container consists of two curved vertical walls and two flat horizontal boundaries. The vertical wavy walls of the enclosure are bounded by the following curves [38]:

- Left wall: $f_1(y) = \left(\frac{1}{2} - \lambda\right) + \lambda\left[1 - \cos\left(\frac{\pi}{2}\left(1 + \frac{4y}{A}\right)\right)\right]$
- Right wall: $f_2(y) = \left(\frac{1}{2} - \lambda\right) - \lambda\left[1 - \cos\left(\frac{\pi}{2}\left(1 + \frac{4y}{A}\right)\right)\right]$

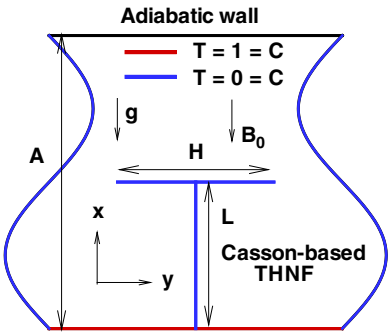

Figure 1: Geometry and boundary of the physical model.

Here, A denotes the height of the cavity, while λ represents the amplitude of the vertical wavy walls of the enclosure. The domain is loaded with a ternary hybrid nanofluid based on a Casson-type non-Newtonian fluid, in which three different nanoparticles are suspended to improve its thermal and solutal transport properties (see Fig. 2). The fluid is influenced by radiation effects, and the enclosure is treated as a porous medium. Heating and concentration are imposed at the lower boundary, while the top boundary is adiabatic. The curved sidewalls are maintained at a uniform low temperature and zero concentration, thereby generating thermal and solutal gradients that drive convection. To further influence the flow inside the cavity, a T-shaped baffle (L is the height of the baffle and H is the length of the head of the baffle) is placed at the center of the lower wall. This baffle acts as an internal obstacle, altering circulation and promoting enhanced mixing. It is assumed that the flow of the trihybrid nanoliquid is two-dimensional, steady, laminar, and incompressible, taking into account viscous influences. The nanofluid is modeled as a non-Newtonian fluid, and it is assumed that the nanoparticles (MWCNT, Cu, and Fe_3O_4) are uniformly dispersed inside the base fluid (water) under local thermal equilibrium conditions, with no slip occurring between the solid and liquid phases. The transport mechanisms in the porous medium are characterized using the Darcy model extended by Brinkman, along with the local thermal equilibrium (LTE) approximation. The no-slip boundary condition is applied for all walls. The effect of thermal radiation is considered in the energy equation; however, Joule heating and viscous dissipation inside the porous medium are neglected. The Boussinesq approximation having opposite and compositional buoyancy forces is taken into account for the body force terms in the y momentum equations and written as $\rho = \rho_0[1-(\beta_\theta)_{thnf}(\theta-\theta_c)-(\beta_c)_{thnf}(c-c_c)]$ where $(\beta_\theta)_{thnf}$ and $(\beta_c)_{thnf}$ are the nanofluid volumetric coefficients of expansion for the thermal and concentration, respectively. It is assumed that all fluid properties are constant except density, which depends on temperature in the buoyancy force. The previously described physical system was simulated by formulating and solving the governing equations in dimensional [36]:

$$\nabla.\mathbf{v}^* = 0 \tag{1}$$

$$\mathbf{v}^*.\nabla\mathbf{v}^* = -\frac{1}{\rho_{thnf}}\nabla P + \frac{\mu_{thnf}}{\rho_{thnf}}\left[1+\frac{1}{\gamma}\right]\nabla^2\mathbf{v}^* - \frac{\mu_{thnf}}{\rho_{thnf}k_f'}\mathbf{v}^* + \mathbf{F}^*, \tag{2}$$

$$\mathbf{v}^*.\nabla\theta = \alpha_{thnf}\nabla^2\theta - \frac{1}{(\rho C_p)_{thnf}}\left[\frac{\partial r_{rx}}{\partial x}+\frac{\partial r_{ry}}{\partial y}\right], \tag{3}$$

$$\mathbf{v}^*.\nabla c = D_{thnf}\nabla^2 c, \tag{4}$$

where $\mathbf{v}^*$ = (u,v) are dimensional velocities along coordinate axes, $F^* = (\mathbf{F_x}, \mathbf{F_y})$ and $\mathbf{F_x} = -\frac{\sigma_{thnf}}{\rho_{thnf}}B_0^2$ u, $\mathbf{F_y} = \frac{g}{\rho_{thnf}}\left[(\rho\beta_\theta)_{thnf}(\theta-\theta_c)-(\rho\beta_c)_{thnf}(c-c_c)\right]$. In the above momentum Eq. (2), γ represents the Casson fluid parameter. In the energy Eq. (3), $-\frac{1}{(\rho C_p)_{thnf}}\left[\frac{\partial r_{rx}}{\partial x}+\frac{\partial r_{ry}}{\partial y}\right]$ is responsible for heat radiation, where, r_{rx} and r_{ry} are written as follows [36,38]:

$$r_{rx} = -\frac{16\sigma^*\theta_c^3}{3\beta_\theta}\frac{\partial\theta}{\partial x}, \quad r_{ry} = -\frac{16\sigma^*\theta_c^3}{3\beta_\theta}\frac{\partial\theta}{\partial y}. \tag{5}$$

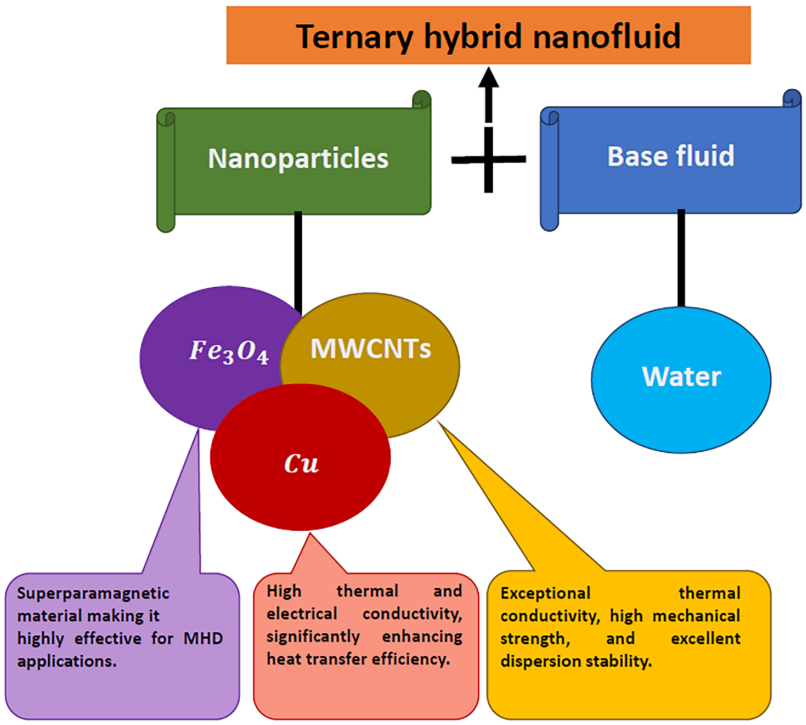

Figure 2: Casson-based ternary hybrid nanofluid with three different nanoparticles.

To nondimensionalize the governing equations, the following dimensionless variables are introduced [36,38]:

$$X = \frac{x}{L},\ Y = \frac{y}{L},\ U = \frac{uL}{\alpha_f},\ V = \frac{vL}{\alpha_f},\ P = \frac{pL^2}{\rho_{thnf}\alpha_f^2},\ T = \frac{\theta - \theta_c}{\theta_h - \theta_c},\ C = \frac{c - c_c}{c_h - c_c}.$$

$$\nabla.\mathbf{V}^* = 0 \tag{6}$$

$$\mathbf{V}^*.\nabla\mathbf{V}^* = -\nabla P + \frac{\nu_{thnf}}{\alpha_f}\left[1 + \frac{1}{\gamma}\right]\nabla^2\mathbf{V}^* - \frac{\nu_{thnf}}{\alpha_f Da}\mathbf{V}^* + \mathbf{F}, \tag{7}$$

$$\mathbf{V}^*.\nabla T = \frac{\alpha_{thnf}}{\alpha_f}\left[1 + \frac{4}{3}Rd\frac{k_f}{k_{thnf}}\right]\nabla^2 T, \tag{8}$$

$$\mathbf{V}^*.\nabla C = \frac{D_{thnf}}{D_f}\frac{1}{Le}\nabla^2 C, \tag{9}$$

where $\mathbf{V}^*$ = (U,V) are velocities along coordinate axes, $\mathbf{F} = (\mathbf{F_X}, \mathbf{F_Y})$ and $\mathbf{F_X} = -\frac{\sigma_{thnf}}{\sigma_f}\frac{\rho_f}{\rho_{thnf}}Ha^2 Pr$ U, $\mathbf{F_Y} = \frac{(\rho\beta_\theta)_{thnf}}{\rho_{thnf}\beta_f}$ Ra Pr (T + N C). The boundary conditions imposed on the governing mathematical model are given in Table 1.

Now, the system of Eqs. (6)–(9) is expressed in terms of the streamfunction (ψ) and vorticity (ζ) variables

$$-\nabla^2\psi = \zeta \tag{10}$$

$$\mathbf{V}^*.\nabla\zeta = \frac{\nu_{thnf}}{\alpha_f}\left(1 + \frac{1}{\gamma}\right)\nabla^2\zeta - \frac{\nu_{thnf}}{\alpha_f Da}\zeta + \frac{(\rho\beta_\theta)_{thnf}}{\rho_{thnf}\beta_f}RaPr\left(\frac{\partial T}{\partial X} + N\frac{\partial C}{\partial X}\right) + \frac{\sigma_{thnf}}{\sigma_f}\frac{\rho_f}{\rho_{thnf}}Ha^2 Pr\frac{\partial U}{\partial Y} \tag{11}$$

$$\mathbf{V}^*.\nabla T = \frac{\alpha_{thnf}}{\alpha_f}\left(1+\frac{4}{3}Rd\frac{k_f}{k_{thnf}}\right)\nabla^2 T, \tag{12}$$

$$\mathbf{V}^*.\nabla C = \frac{D_{thnf}}{D_f}\frac{1}{Le}\nabla^2 C, \tag{13}$$

where,

$$U = \frac{\partial\psi}{\partial Y}, \quad V = -\frac{\partial\psi}{\partial X}, \zeta = \frac{\partial V}{\partial X} - \frac{\partial U}{\partial Y}, \tag{14}$$

where the non-dimensional parameters are listed in Table 2.

Table 1: The applied boundary conditions are expressed in dimensionless form.

Walls	Boundary Conditions			
	Velocities (*U*, *V*)	**Temperature (*T*)**	**Concentration (*C*)**	**Vorticity (ζ)**
Top	No-slip boundary ($U = 0 = V$)	Adiabatic $\left(\frac{\partial T}{\partial Y} = 0\right)$	Adiabatic $\left(\frac{\partial C}{\partial Y} = 0\right)$	$\zeta = -\frac{\partial^2\psi}{\partial Y^2}$
Left and right	No-slip boundary ($U = 0 = V$)	Cold ($T = 0$)	Low concentration ($C = 0$)	$\zeta = -\frac{\partial^2\psi}{\partial n^2}$
Bottom	No-slip boundary ($U = 0 = V$)	Hot ($T = 1$)	High concentration ($C = 1$)	$\zeta = -\frac{\partial^2\psi}{\partial Y^2}$
Baffle	No-slip boundary ($U = 0 = V$)	Cold ($T = 0$)	Low concentration ($C = 0$)	$\zeta = -\frac{\partial^2\psi}{\partial n^2}$

Table 2: Dimensionless parameters with their ranges and sign conventions.

Parameters	Non-Dimensional Form	Values	Sign Convention
Rayleigh Number (Ra)	$\frac{g\beta_f(\theta_h-\theta_c)L^3}{\nu_f\alpha_f}$	$10^4 \le Ra \le 10^6$	always $Ra > 0$
Lewis number (Le)	$\frac{\alpha_f}{D_f}$	$1 \le Le \le 20$	always $Le > 0$
Darcy number (Da)	$\frac{k'_f}{L^2}$	$10^{-5} \le Da \le 10^{-3}$	always $Da > 0$
Hartmann number (Ha)	$B_0 L\sqrt{\frac{\sigma_f}{\rho_f\nu_f}}$	$0 \le Ha \le 100$	always $Ha \ge 0$
Radiation parameter (Rd)	$\frac{4\sigma^*\theta_c^3}{k_f\beta_\theta}$	$1 \le Rd \le 5$	$Rd > 0$
Buoyancy ratio (N)	$\frac{(\beta_c)_{thnf}(c_h-c_c)}{(\beta_\theta)_{thnf}(\theta_h-\theta_c)}$	1	$N > 0$ (aiding flow)

2.1 Ternary Nanofluid Property Model

The ternary nanofluid utilized in this study combines thermally and electrically conductive multi-walled carbon nanotubes (MWCNTs), highly conductive Copper (Cu), and magnetic oxide (Fe_3O_4) nanoparticles, offering a unique blend of properties that enhance stability, heat transfer efficiency, and thermal conductivity. Table 3 summarizes the thermophysical properties of the base fluid and the nanoparticles (MWCNT, Cu, Fe_3O_4). In this work, the effective density, the effective viscosity, the specific heat capacitance, the thermal expansion coefficient, the thermal conductivity, the thermal diffusivity, and the solutal diffusivity of the ternary hybrid nanoliquids are obtained from the following relations [36]:

- Density: $\rho_{thnf} = (1-\phi_3)\left[(1-\phi_2)\left\{(1-\phi_1)\rho_f + \phi_1\rho_{s1}\right\} + \phi_2\rho_{s2}\right] + \phi_3\rho_{s3}$
- Viscosity: $\dfrac{\mu_{thnf}}{\mu_f} = (1-\phi_1)^{-2.5}(1-\phi_2)^{-2.5}(1-\phi_3)^{-2.5}$
- Specific heat capacity: $(\rho c_p)_{thnf} = (1-\phi_3)\left[(1-\phi_2)\left\{(1-\phi_1)(\rho c_p)_f + \phi_1(\rho c_p)_{s1}\right\} + \phi_2(\rho c_p)_{s2}\right] + \phi_3 (\rho c_p)_{s3}$
- Thermal expansion coefficient: $(\rho\beta)_{thnf} = (1-\phi_3)\left[(1-\phi_2)\left\{(1-\phi_1)(\rho\beta)_f + \phi_1(\rho\beta)_{s1}\right\} + \phi_2(\rho\beta)_{s2}\right] + \phi_3(\rho\beta)_{s3}$
- Thermal conductivity:

$$\frac{k_{thnf}}{k_{hnf}} = \frac{k_{s3} + 2k_{hnf} + 2\phi_3\left(k_{s3} - k_{hnf}\right)}{k_{s3} + 2k_{hnf} - \phi_3\left(k_{s3} - k_{hnf}\right)}, \text{ where, } \frac{k_{hnf}}{k_{nf}} = \frac{k_{s2} + 2k_{nf} + 2\phi_2\left(k_{s2} - k_{nf}\right)}{k_{s2} + 2k_{nf} - \phi_2\left(k_{s2} - k_{nf}\right)},$$

$$\text{and } \frac{k_{nf}}{k_f} = \frac{k_{s1} + 2k_f + 2\phi_1\left(k_{s1} - k_f\right)}{k_{s1} + 2k_f - \phi_1\left(k_{s1} - k_f\right)}$$

- Thermal diffusivity: $\alpha_{thnf} = \dfrac{k_{thnf}}{(\rho C_p)_{thnf}}$
- Electrical conductivity:

$$\frac{\sigma_{thnf}}{\sigma_{hnf}} = \frac{\sigma_{s2} + 2\sigma_{hnf} + 2\phi_2\left(\sigma_{s2} - \sigma_{hnf}\right)}{\sigma_{s2} + 2\sigma_{hnf} - \phi_2\left(\sigma_{s2} - \sigma_{hnf}\right)}, \quad \text{where,} \quad \frac{\sigma_{hnf}}{\sigma_{nf}} = \frac{\sigma_{s2} + 2\sigma_{nf} + 2\phi_2\left(\sigma_{s2} - \sigma_{nf}\right)}{\sigma_{s2} + 2\sigma_{nf} - \phi_2\left(\sigma_{s2} - \sigma_{nf}\right)}, \quad \text{and,}$$

$$\frac{\sigma_{nf}}{\sigma_f} = \frac{\sigma_{s1} + 2\sigma_f + 2\phi_1\left(\sigma_{s1} - \sigma_f\right)}{\sigma_{s1} + 2\sigma_f - \phi_1\left(\sigma_{s1} - \sigma_f\right)}$$

- Solutal diffusivity: $D_{thnf} = (1-\phi_1)(1-\phi_2)(1-\phi_3)D_f$

where the suffixes f, nf, and hnf denote base fluid, nanoliquid, and hybrid nanoliquid, respectively. Here ϕ_1, ϕ_2, and ϕ_3 are volume fractions of MWCNTs ($s1$), Cu ($s2$), and Fe_3O_4 ($s3$) nanoparticles, respectively. In this study, the nanoparticle volume fractions are prescribed as $\phi_1 = 0.01$, $\phi_2 = 0.02$, and $\phi_3 = 0.01$, corresponding to 25%, 50%, and 25% of the total solid loading, respectively.

Table 3: Thermophysical properties of H_2O, MWCNT, Cu, Fe_3O_4 [38].

Physical Properties	Water	MWCNT (*s*1)	Cu (*s*2)	Fe_3O_4 (*s*3)
ρ (Kg m^{-3})	997.1	1600	8933	5200
C_p (J Kg^{-1} K^{-1})	4179	796	385	670
k (W m^{-1} K^{-1})	0.613	3000	401	6
β (K^{-1})	21×10^{-5}	4.2×10^{-5}	1.67×10^{-5}	1.3×10^{-5}
σ (Sm^{-1})	5×10^{-6}	10^6	5.96×10^7	0.3
μ (Kg m^{-1}s^{-1})	8.9×10^{-4}	–	–	–

3 Thermal and Solutal Performance

In this study, the energy and species transport inside the cavity are calculated by the following equation:

$$Nu_{\text{avg}} = \frac{k_{thnf}}{k_f}\left(1+\frac{4}{3}Rd\frac{k_f}{k_{thnf}}\right)\int_0^1\left(-\frac{\partial T}{\partial Y}\right)dX.$$
$$Sh_{\text{avg}} = \frac{D_{thnf}}{D_f}\int_0^1\left(-\frac{\partial C}{\partial Y}\right)dX. \tag{15}$$

Using the Simpson 1/3 method, the numerical integration of Eq. (15) is carried out. These parameters (dimensionless) help to understand the behavior of the heat and solute transport within the container.

4 The Entropy Generation

In this research, entropy generation analysis is executed to assess the irreversibilities arising from mass diffusion, magnetic field effects, fluid friction, and thermal transport within the enclosure. The dimensional form of local entropy generation for this analysis is expressed as follows [36,38]:

$$\underbrace{\frac{k_{thnf}}{\theta_0^2}\left[(\theta_x)^2+(\theta_y)^2\right]}_{\text{Entropy generation due heat transfer}(E_{l.h.t})} + \underbrace{\left(1+\frac{1}{\gamma}\right)\frac{\mu_{thnf}}{\theta_0}\left[2(u_x)^2+2(v_y)^2+(u_y+v_x)^2+\frac{1}{k_f'}\left(u^2+v^2\right)\right]}_{\text{Entropy generation due fluid friction}(E_{l.f.f})}$$
$$+\underbrace{\frac{\sigma_{thnf}}{\theta_0}u^2}_{\text{Entropy generation due magnetic field}(E_{l.m.f})} + \underbrace{\frac{RD_{thnf}}{c_o}\left[(c_X)^2+(c_Y)^2\right]+\frac{RD_{thnf}}{\theta_0}\left[\theta_x c_x+\theta_y c_y\right]}_{\text{Entropy generation due mass transfer}(E_{l.m.t})} \tag{16}$$

By employing $\left(\frac{k_f\Delta\theta^2}{\theta_0^2L^2}\right)$ as typical scales, the dimensionless form of local entropy generation numbers are written as follows:

$$E_{gen} = \frac{k_{thnf}}{k_f}\left[(T_X)^2+(T_Y)^2\right]+\varphi_1\left(1+\frac{1}{\gamma}\right)\frac{\mu_{thnf}}{\mu_f}\left[2(U_X)^2+2(V_Y)^2+(U_Y+V_X)^2\right.$$
$$\left.+\frac{1}{Da}\left(U^2+V^2\right)\right]+\varphi_1\frac{\sigma_{thnf}}{\sigma_f}Ha^2U^2+\varphi_2\frac{D_{thnf}}{D_f}\left[(C_X)^2+(C_Y)^2\right]$$
$$+\varphi_3\frac{D_{thnf}}{D_f}\left[T_XC_X+T_YC_Y\right] \tag{17}$$

where, $\varphi_1 = \frac{\mu_f \theta_0}{k_f}\left[\frac{\alpha_f}{L(\theta_h-\theta_c)}\right]^2$, $\varphi_2 = \frac{RD_f}{k_f c_0}\left(\theta_0 \frac{c_h-c_l}{\theta_h-\theta_c}\right)^2$ and $\varphi_3 = \frac{RD_f}{k_f}\left(\theta_0 \frac{c_h-c_l}{\theta_h-\theta_c}\right)$. For this simulation, $\varphi_1 = 10^{-4}$, $\varphi_2 = 0.5$ and $\varphi_3 = 10^{-2}$ are irreversibility ratio ([36,38]). In addition, the total entropy generation (E_T) is measured by

$$E_T = E_{HT} + E_{FF} + E_{MF} + E_{MT}, \tag{18}$$

where, $E_{HT} = \int_\Omega E_{lht}\ d\Omega$, $E_{FF} = \int_\Omega E_{lff}\ d\Omega$, $E_{MF} = \int_\Omega E_{lmf}\ d\Omega$, and $E_{MT} = \int_\Omega E_{lmt}\ d\Omega$. In addition, the Bejan number (Be) is defined as follows [36,38]:

$$Be = \frac{E_{HT} + E_{MT}}{E_T}. \tag{19}$$

It is noted that $Be > 0.5$ and $Be < 0.5$ indicate the dominance of thermal transport and fluid friction irreversibility, respectively.

5 Solution Procedure

Using an algebraic transformation, the transformation of a physical domain (x, y) into a computational domain (ξ, η) is attained. The transformation are constituted as

$$\begin{aligned} Y &= \xi, \\ X &= F_1(\eta)(2\xi + 1), \end{aligned} \tag{20}$$

where, $F_1(\eta) = \left(\frac{1}{2} - \lambda\right) + \lambda\left[1 - \cos\left(\frac{\pi}{2}\left(1 + \frac{4\eta}{A}\right)\right)\right]$. Here, A denotes the cavity height, while λ represents the amplitude of the vertical wavy walls of the enclosure. The first- and second-order differential operators can be represented in compact matrix form as:

- First order:

$$\begin{bmatrix} \partial_x \\ \partial_y \end{bmatrix} = \frac{1}{|J|}\begin{bmatrix} y_\eta & -y_\xi \\ -x_\eta & x_\xi \end{bmatrix}\begin{bmatrix} \partial_\xi \\ \partial_\eta \end{bmatrix}, \tag{21}$$

- Second order:

$$\begin{bmatrix} \partial_{xx} \\ \partial_{yy} \end{bmatrix} = \frac{1}{|J|^2}\mathbf{A}\begin{bmatrix} \partial_\xi \\ \partial_\eta \end{bmatrix} + \frac{1}{|J|^2}\mathbf{B}\begin{bmatrix} \partial_{\xi\xi} \\ \partial_{\xi\eta} \\ \partial_{\eta\eta} \end{bmatrix}, \tag{22}$$

where the coefficient matrices are outlined as

$$\mathbf{A} = \begin{bmatrix} y_\eta & -y_\xi & 0 & 0 \\ 0 & 0 & x_\xi & x_\eta \end{bmatrix}\begin{bmatrix} y_{\xi\eta} & -y_{\xi\xi} \\ y_{\eta\eta} & -y_{\xi\eta} \\ x_{\xi\eta} & x_{\xi\eta} \\ x_{\eta\eta} & -x_{\xi\xi} \end{bmatrix}, \tag{23}$$

$$\mathbf{B} = \begin{bmatrix} y_\eta^2 & -2y_\xi y_\eta & y_\xi^2 \\ x_\eta^2 & -2x_\xi x_\eta & x_\xi^2 \end{bmatrix}. \tag{24}$$

The Jacobian of the transformation is given by:

$$J = x_\xi y_\eta - x_\eta y_\xi. \tag{25}$$

The governing Eqs. (10)–(13) are transformed into the following generalized form:

$$a\frac{\partial^2\widehat{\Phi}}{\partial\xi^2}+g\frac{\partial^2\widehat{\Phi}}{\partial\xi\partial\eta}+b\frac{\partial^2\widehat{\Phi}}{\partial\eta^2}+c\frac{\partial\widehat{\Phi}}{\partial\xi}+d\frac{\partial\widehat{\Phi}}{\partial\eta}+p\widehat{\Phi}=f, \tag{26}$$

The central finite difference approximations are applied for spatial discretization, and their formulations are listed in Table 4.

Table 4: Finite difference approximations for first and second order derivatives.

Derivative	Finite Difference Approximation
$\delta_\xi\widehat{\Phi}_{i,j}$	$\frac{1}{2h}\left(\widehat{\Phi}_{i+1,j}-\widehat{\Phi}_{i-1,j}\right)$
$\delta_\xi^2\widehat{\Phi}_{i,j}$	$\frac{1}{h^2}\left(\widehat{\Phi}_{i+1,j}-2\widehat{\Phi}_{i,j}+\widehat{\Phi}_{i-1,j}\right)$
$\delta_\eta\widehat{\Phi}_{i,j}$	$\frac{1}{2k}\left(\widehat{\Phi}_{i,j+1}-\widehat{\Phi}_{i,j-1}\right)$
$\delta_\eta^2\widehat{\Phi}_{i,j}$	$\frac{1}{k^2}\left(\widehat{\Phi}_{i,j+1}-2\widehat{\Phi}_{i,j}+\widehat{\Phi}_{i,j-1}\right)$
$\delta_\xi\delta_\eta\widehat{\Phi}_{i,j}$	$\frac{1}{4hk}\left(\widehat{\Phi}_{i+1,j+1}-\widehat{\Phi}_{i-1,j+1}-\widehat{\Phi}_{i+1,j-1}+\widehat{\Phi}_{i-1,j-1}\right)$

The higher-order mixed derivative terms are evaluated using compact finite difference schemes, given by:

$$\delta_\xi^2\delta_\eta(\widehat{\Phi}_\xi)_{i,j}=\frac{1}{2h^2k}\left[2(\widehat{\Phi}_\xi)_{i,j-1}-2(\widehat{\Phi}_\xi)_{i,j+1}-(\widehat{\Phi}_\xi)_{i-1,j-1}-(\widehat{\Phi}_\xi)_{i+1,j-1}+(\widehat{\Phi}_\xi)_{i+1,j+1}+(\widehat{\Phi}_\xi)_{i-1,j+1}\right]. \tag{27}$$

$$\delta_\xi\delta_\eta^2(\widehat{\Phi}_\eta)_{i,j}=\frac{1}{2hk^2}\left[2(\widehat{\Phi}_\eta)_{i-1,j}-2(\widehat{\Phi}_\eta)_{i+1,j}-(\widehat{\Phi}_\eta)_{i-1,j-1}+(\widehat{\Phi}_\eta)_{i+1,j-1}+(\widehat{\Phi}_\eta)_{i+1,j+1}-(\widehat{\Phi}_\eta)_{i-1,j+1}\right]. \tag{28}$$

The first-order derivatives are approximated using a compact Padé finite difference scheme, given by:

$$\frac{1}{6}(\widehat{\Phi}_\xi)_{i+1,j}+\frac{4}{6}(\widehat{\Phi}_\xi)_{i,j}+\frac{1}{6}(\widehat{\Phi}_\xi)_{i-1,j}=\frac{\widehat{\Phi}_{i+1,j}-\widehat{\Phi}_{i-1,j}}{2h}. \tag{29}$$

$$\frac{1}{6}(\widehat{\Phi}_\eta)_{i,j+1}+\frac{4}{6}(\widehat{\Phi}_\eta)_{i,j}+\frac{1}{6}(\widehat{\Phi}_\eta)_{i,j-1}=\frac{\widehat{\Phi}_{i,j+1}-\widehat{\Phi}_{i,j-1}}{2k}. \tag{30}$$

The governing Eqs. (10)–(13) are spatially discretized using a recently developed higher-order compact (HOC) scheme, as proposed in [39–42]. The resulting linear systems are solved using the BiCGStab algorithm [43]. The iteration ends when the difference in values between successive steps becomes very small and stays within a defined limit:

$$\max\left|\Upsilon_{i,j}^{(\delta+1)}-\Upsilon_{i,j}^{(\delta)}\right|<0.5\times10^{-5}, \tag{31}$$

where the matrix $\boldsymbol{\Upsilon}$ represents the discretized variables:

$$\boldsymbol{\Upsilon}=\begin{bmatrix}\psi_{i,j} & \zeta_{i,j} & T_{i,j} & C_{i,j}\end{bmatrix}^T. \tag{32}$$

This confirms that the numerical solutions for ψ, ζ and T have converged within the acceptable range of accuracy. The procedural outline is given in Table 5. This iterative cycle is repeated until the full set of coupled equations converges within the specified tolerance. The mathematical demonstration of the model and the flowchart of the solution algorithm are shown in Figs. 3 and 4, respectively. The number of iterations required for convergence for different values of Ra is displayed in Table 6.

Table 5: Numerical solution procedure for steady-state flow and transport fields.

Step	Description
1	Initialize flow variables: ψ, ζ, T, C, u, v
2	Apply boundary conditions for all variables and their spatial derivatives
3	Solve discrete equations iteratively using BiCGStab:
	(a) Update $T^{(\gamma+1)}$ using $u^{(\gamma)}, v^{(\gamma)}$ and spatial gradients
	(b) Update $C^{(\gamma+1)}$ similarly
	(c) Update $\zeta^{(\gamma+1)}$ using velocity and temperature/concentration gradients
	(d) Solve for $\psi^{(\gamma+1)}$ using updated values
	(e) Compute $u^{(\gamma+1)}, v^{(\gamma+1)}$ from ψ derivatives
4	Check convergence of all variables:
	If $\max \left\lvert \Upsilon^{(\gamma+1)} - \Upsilon^{(\gamma)} \right\rvert <$ Tol, stop; otherwise, repeat from Step 2

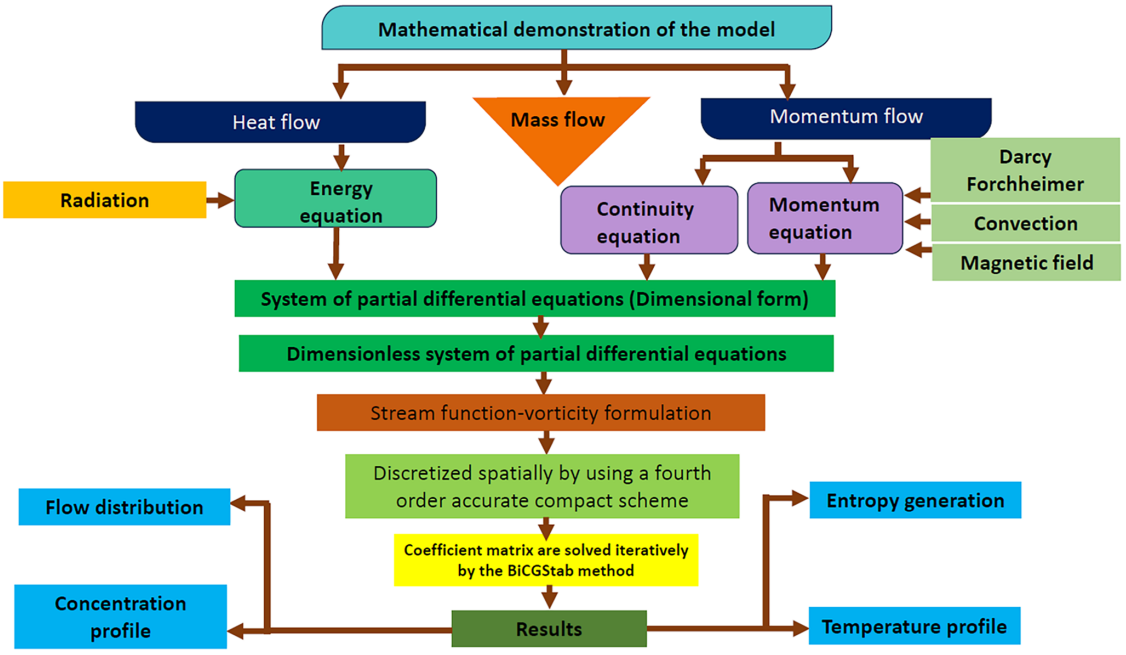

Figure 3: Model simulation.

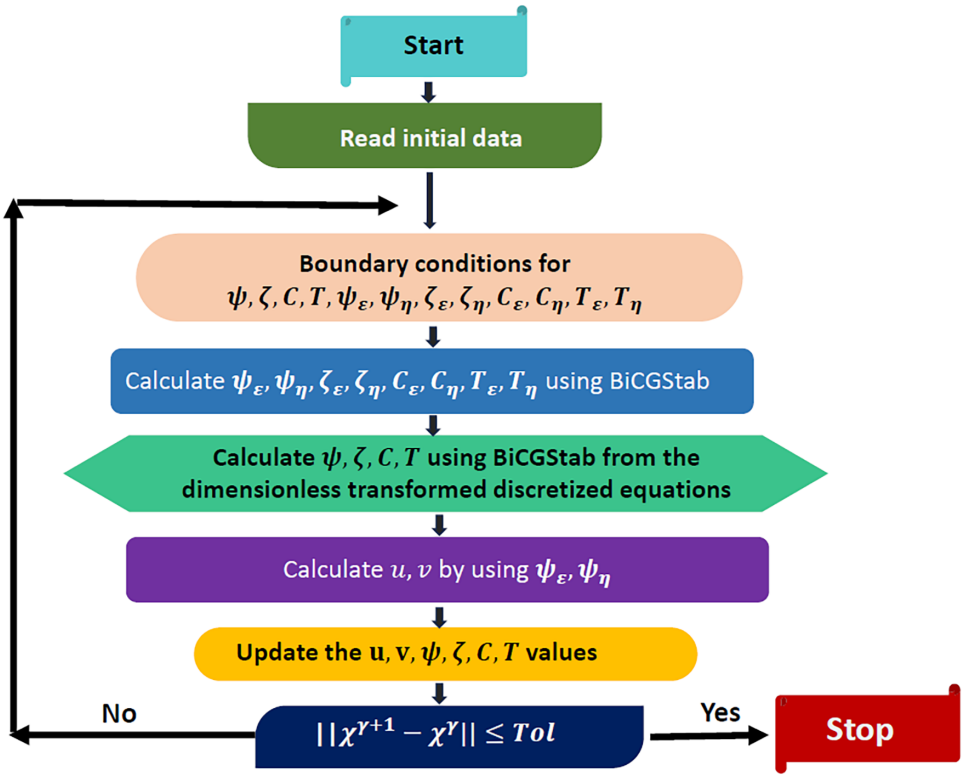

Figure 4: Flow chart for solution algorithm.

Table 6: The number of iterations required for convergence for different values of Ra and γ.

Ra	$\gamma = 0.1$	$\gamma = 1$	$\gamma = 10$
10^4	17,372	16,366	10,391
10^5	16,348	18,124	15,099
10^6	24,021	27,148	34,217

6 Code Validation and Grid-Independent Study

The in-house numerical code developed for this research has been validated against established literature, including both numerical and experimental results from reputed publications. Table 7 presents an analogy between the $\psi_{\min}$ values from the results of Al-Amiri et al. [44] and those of our study. The data in the table shows that our code performs well and produces steady, correct results with previous studies. In addition, Table 8 displays an analogy of Sh_{avg} and Nu_{avg} on the heated bottom wall, as Bettaibi et al. [45], for $Le = 1$, $Pr = 1$, $Re = 10^2$ and $Gr = 10^2$. An analogy shows that our custom-built code can correctly solve the double-diffusion behaviors. We reproduced the results of Sompong and Witayangkurn [46] for the flow field and temperature distributions, as illustrated in Fig. 5. The close agreement confirms that the present code accurately predicts transport phenomena in a wavy porous cavity. In Fig. 6, the present in-house code is validated against the results of Pandit et al. [47]. The streamline and isotherm contours show excellent agreement, confirming the accuracy and reliability of the numerical model for MHD flow in a wavy enclosure. An analogy of Nu_{avg} for different concentrations of nanofluids (ϕ), Prandtl numbers (Pr_{nf}), and Rayleigh numbers (Ra_{nf}), in Table 9. The calculated values of Nu_{avg} completely coincide with

previous research [48,49], revealing that the system is reliable for understanding thermal transport. In the section, Fig. 7 shows an analogy of the flow structure and energy spread in a U-shaped container with a baffle, which is in strong correlation with the results stated by Ma et al. [50]. As shown in Fig. 8, the verification of the computational code was performed based on the findings of Arefmanesh et al. [51] for a cavity with a rectangular baffle. This correlation shows that the model can exactly capture baffle-related flow and thermal transport, which makes it reliable. Fig. 9 shows one more graph of entropy generation, which reveals a strong correlation with the results stated by Ilis et al. [52]. Our results are in good correlation with previous studies, which show that our computational approach is trustworthy and accurate. An analogy shows that our custom-built code can correctly solve thermal problems under different conditions. It regularly produces promising results and may be used for research and further analysis.

Table 7: Compares the result of Al-Amiri et al. [44] study with present study of minimum values of streamfunction (ψ_{min}) for different values of N with Re = 100, Ri = 0.01, Le = 1 and Pr = 1 between.

N	−100	−50	−25	0	25	50	100
Present study	−0.0828	−0.0906	−0.0966	−0.1037	−0.1111	−0.1194	−0.1363
Al-Amiri et al. [44]	−0.0813	−0.0893	−0.0953	−0.1034	−0.1125	−0.1172	−0.1349

Table 8: Compares the result of Bettaibi et al. [45] study with the present study of average Nusselt and Sherwood numbers at the hot bottom wall between the and for Gr = 100, Re = 100, Pr = 1, Le = 1.

	Nu_{avg}			Sh_{avg}		
N	Present Study	Bettaibi et al. [45]	Error (%)	Present Study	Bettaibi et al. [45]	Error (%)
−20	1.366	1.366	0.0	1.366	1.366	0.0
0	2.316	2.401	3.67	2.316	2.401	3.67
20	3.240	3.477	7.31	3.240	3.477	7.31

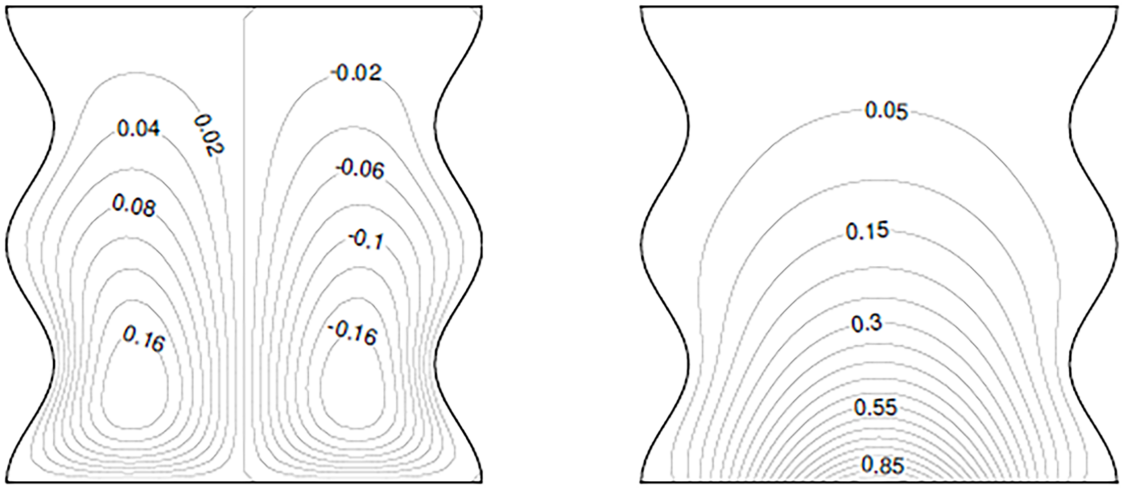

(a)

Figure 5: (Continued)

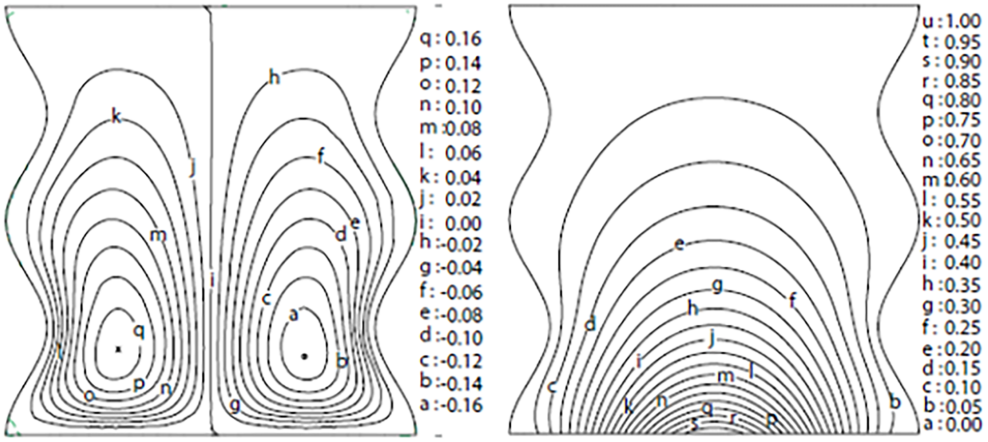

(b)

Figure 5: Comparison of streamlines and isotherm contours inside a vertical wavy porous enclosure: (**a**) present (**b**) Sompong and Witayangkurn [46].

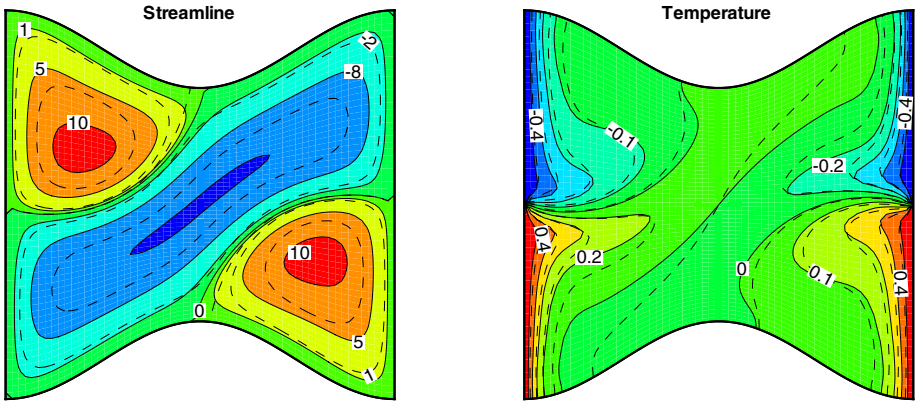

(a)

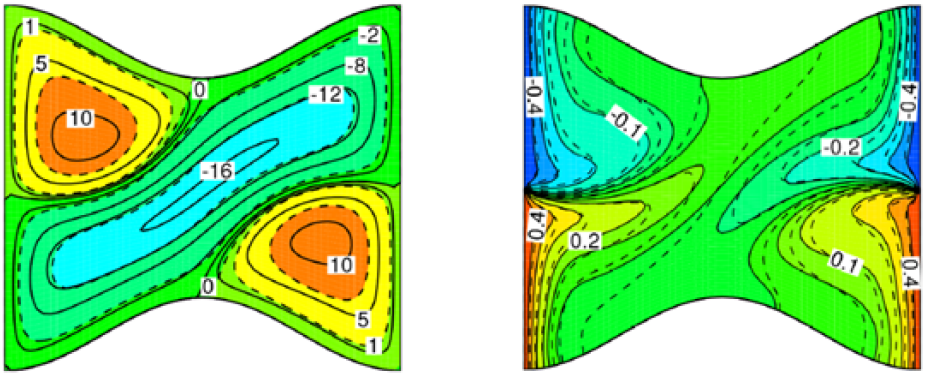

(b)

Figure 6: Streamline and temperature contours: (**a**) Present study, (**b**) Pandit et al. [47].

Table 9: Comparison of $\overline{Nu}$ between the experimental results, various numerical techniques and the present work for various ϕ, Ra_{nf} and Pr_{nf}.

$\overline{Nu}$	ϕ = 1% $Ra_{nf} = 7.74547 \times 10^7$ $Pr_{nf} = 7.0659$	ϕ = 2% $Ra_{nf} = 6.675118 \times 10^7$ $Pr_{nf} = 7.3593$	ϕ = 3% $Ra_{nf} = 5.6020687 \times 10^7$ $Pr_{nf} = 7.8353$
Exp [48]	32.2037	31.0905	29.0769
FEM-2D [49]	31.8633	31.6085	28.2160
FEM-3D [49]	32.7829	32.1833	31.3692
FDM-2D [49]	30.6570	30.5030	30.2050
LBM-2D [49]	30.0010	29.8370	29.6180
Present result	32.0521	31.2089	30.1379

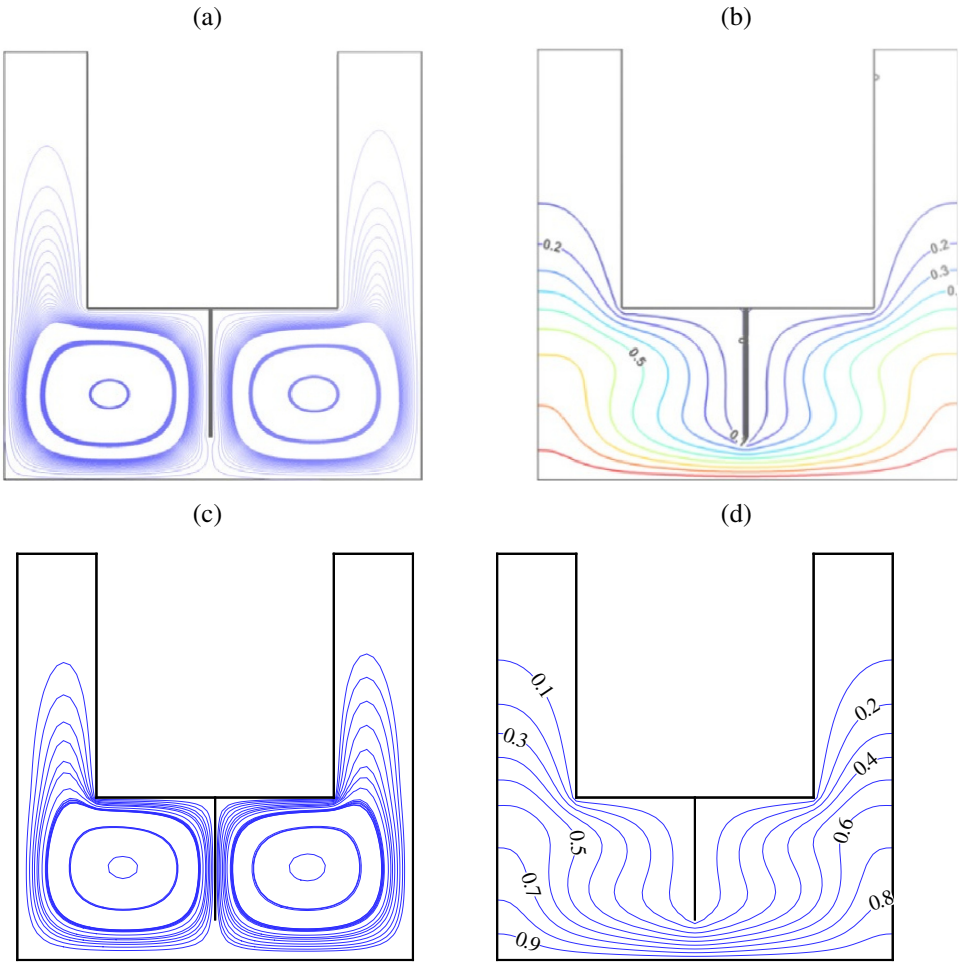

Figure 7: Compares (i) a result of Ma et al. [50] (**a**,**b**) with and (ii) present study (**c**,**d**) for $\phi = 0.05$, $Ra = 10^5$, $AR = 0.6$, Ha = 20.

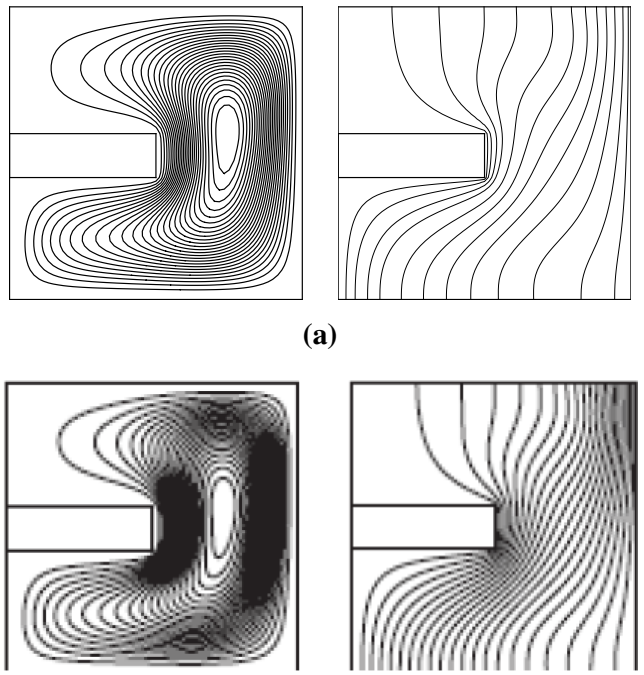

Figure 8: Compares (**a**) an effect of the present study with (**b**) Arefmanesh et al. [51] study. It explores streamlines and isotherms within an enclosure containing a rectangular baffle.

As illustrated in Table 10, a grid independence test was carried out using 31 × 31, 61 × 61, and 121 × 121 meshes. The results indicate that the variation in Nu_{avg} and Sh_{avg} between the 61 × 61 and 121 × 121 grids is negligible, confirming that the 61 × 61 mesh provides sufficient accuracy with reasonable computational cost. Together with the validation study, this confirms the accuracy and reliability of the numerical code.

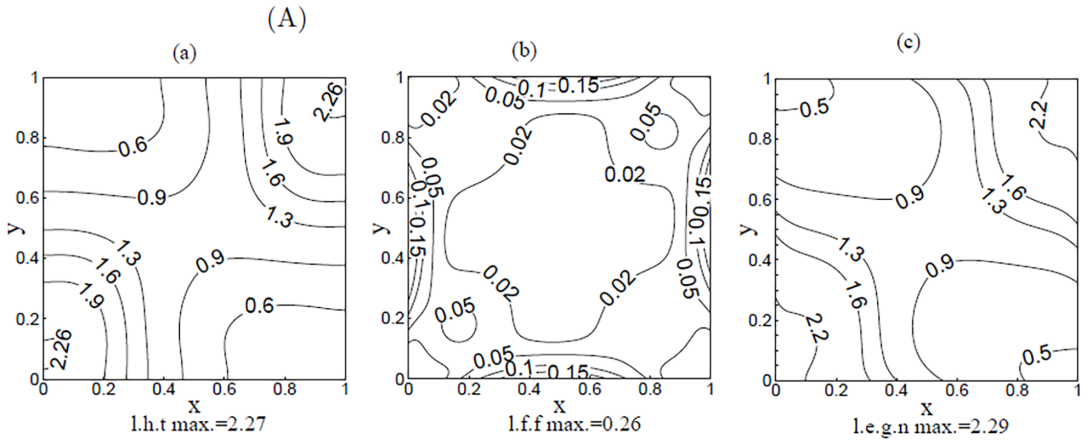

Figure 9: (Continued)

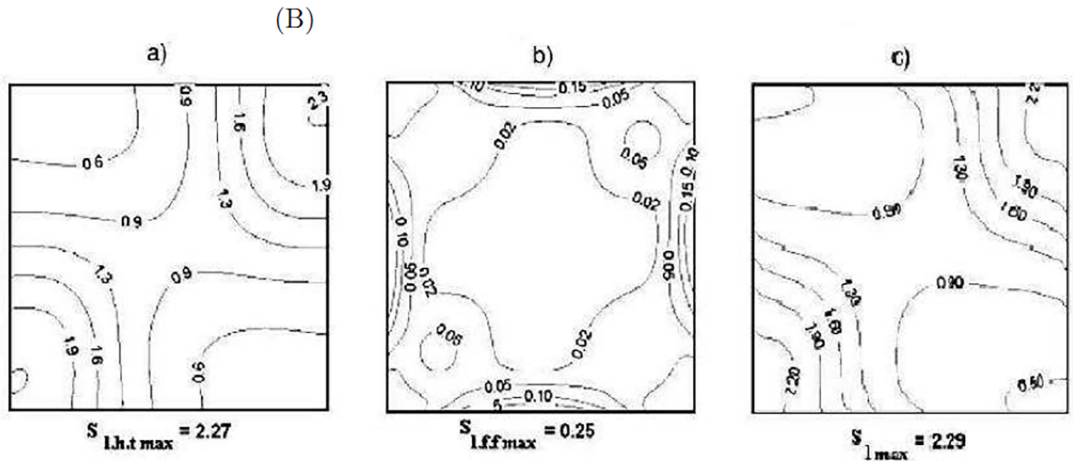

Figure 9: Compares (**A**) an effect of the present study with (**B**) a previous study [52]. It explores three aspects: (**a**) entropy generation due to thermal transport (**b**) entropy generation due to fluid friction and (**c**) total entropy generation number for an enclosure with a cold left and right walls with an adiabatic top and hot bottom walls at $Ra = 10^3$ for $Pr = 6.2$.

Table 10: Grid independence study of the problem for three different grid sizes 31 × 31, 61 × 61 and 121 × 121.

Ra	Grid	Nu_{avg}	Sh_{avg}
10^4	31 × 31	13.266	5.176
	61 × 61	25.683	10.143
	121 × 121	25.824	10.213
10^6	31 × 31	22.911	24.438
	61 × 61	36.470	16.833
	121 × 121	36.512	16.925

7 Results and Discussion

This part presents an in-depth analysis of the numerical results, highlighting the practical understanding gained from the study. Using a Casson-based MWCNT-Cu-Fe_3O_4-H_2O (ternary hybrid nanofluid) nanofluid, this study examines how thermal and solute are transported within a cavity. The geometry has been made complex by placing a baffle (T-shaped) in the middle of the bottom wall. Additionally, this work examines how the combined effects of three different nanoparticles, a Casson fluid, and a specific thermal condition impact the system under various situations. The effects of various key parameters: Rayleigh number ($10^4 \leq Ra \leq 10^6$), Lewis number ($1 \leq Le \leq 20$), radiation parameter ($1 \leq Rd \leq 5$), buoyancy ratio ($N = 1$), Darcy number ($10^{-5} \leq Da \leq 10^{-3}$), and solid particle concentration ($0.0 \leq \phi_{thnp} \leq 0.04$) on solutal and thermal distributions, entropy generation, and the Bejan number are thoroughly analyzed. These results indicate that the internal baffle and nanofluids help to enhance the thermal and solute transport inside the enclosure, which can be used for thermal regulation.

In Fig. 10, we provide a detailed analysis of flow pattern, thermal, and solutal performance between "without baffle" and "with baffle" for Ra = 10^6. In the absence of a T-shaped baffle, two rotating flow loops form within the enclosure. This happens due to the temperature difference. The ternary hybrid nanofluid increases from the heated lower boundary and moves downward along the cold vertical boundaries. This creates two vortices within the enclosure, one rotating clockwise and the other counterclockwise. When

a T-shaped baffle is added, the downward flow near the cold boundaries is affected. The baffle divides and redirects the rising fluid, containing several smaller circulation vortices within the wavy enclosure. This different flow dynamic occurs because the T-shaped baffle obstructs the motion of the ternary hybrid nanofluid. The inclusion of a T-shaped baffle suppresses the flow, which reduces the thermal and solutal transport rates. The thermal line shows symmetry with respect to the vertical line, consistent with the symmetrical flow pattern. This symmetry occurs from the joint effects of viscous and buoyancy forces, which produce two primary vortices. Therefore, these results highlight the important role of the T-shaped baffle in altering the isotherm and concentration contours, thus modifying the heat and solutal transport performance of the wavy enclosure.

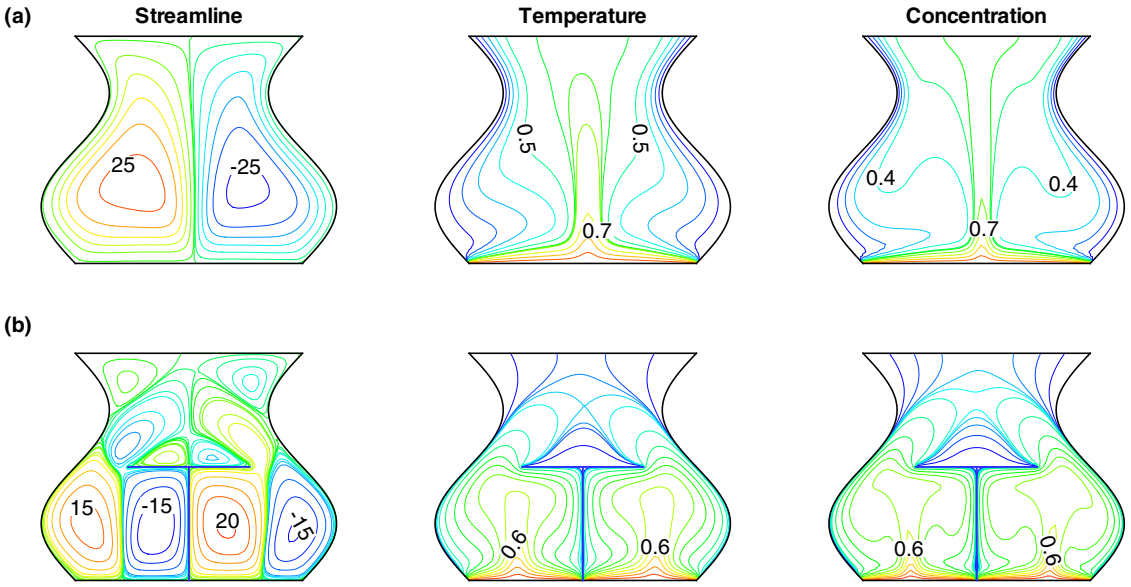

Figure 10: Streamline, temperature, and concentration contours for $Le = 1$, $Rd = 1$, $Da = 10^{-3}$, $Ha = 10$: (**a**) without baffle (**b**) with baffle.

In Table 11, a quantitative comparison of Nu_{avg}, Sh_{avg}, E_T, and Be is presented for configurations with and without a T-shaped baffle over a range of Rayleigh numbers (Ra). The results indicate that heat transfer, mass transport, and E_T increase with increasing Ra in both cases, whereas the Bejan number decreases. Furthermore, the configuration incorporating the T-shaped baffle consistently exhibits superior thermal and solutal performance compared to the cavity without a baffle. Therefore, the inclusion of a T-shaped baffle within the enclosure enhances overall convective transport characteristics and system performance.

Table 11: Quantitative comparison of average Nusselt number (Nu_{avg}), average Sherwood number (Sh_{avg}), total entropy generation, and Bejan number for cases with and without a T-shaped baffle.

Ra	**Without T-Shaped Baffle**			**With T-Shaped Baffle**		
	$\mathbf{10^4}$	$\mathbf{10^5}$	$\mathbf{10^6}$	$\mathbf{10^4}$	$\mathbf{10^5}$	$\mathbf{10^6}$
Nu_{avg}	14.275	16.202	26.832	25.682	26.522	39.030
Sh_{avg}	5.384	7.840	14.162	9.798	11.457	20.288
E_T	7.016	128.105	4101.105	23.519	68.997	2538.818
Be	0.987	0.087	0.004	0.991	0.354	0.013

As demonstrated in Fig. 11, the variation of (i) the average Nusselt number Nu_{avg} and (ii) the average Sherwood number Sh_{avg} with the volume fraction of nanoparticles (ϕ) is presented for mono nanofluid, hybrid nanofluid and ternary hybrid nanofluid. An increase in ϕ leads to an increase and decrease in Nu_{avg} and Sh_{avg}, respectively, as shown in Fig. 11. However, both Nu_{avg} and Sh_{avg} are consistently higher in the presence of a ternary hybrid nanofluid than in mono- and hybrid nanofluids for a fixed ϕ. Therefore, it can be concluded that the incorporation of ternary hybrid nanofluid significantly enhances thermal and solutal transport performance compared to mono and hybrid nanofluids. The ternary hybrid nanofluid significantly reduces the solutal transport performance compared to mono and hybrid nanofluids as ϕ increases. In general, this analysis highlights the significant role of the ternary hybrid nanofluid in enhancing the values of Nu_{avg} and Sh_{avg}, thus improving the thermal and species characteristics within the system.

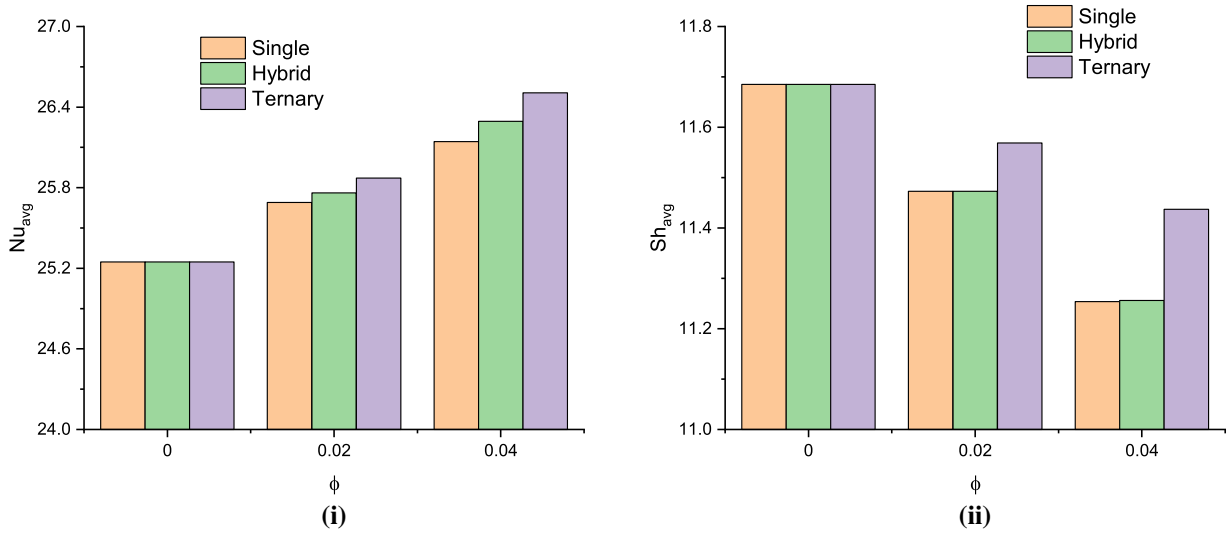

Figure 11: Comparison of (**i**) average Nusselt number (Nu_{avg}) and (**ii**) average Sherwood number (Sh_{avg}) for single nanofluid, hybrid nanofluid, and ternary hybrid nanofluid cases.

Fig. 12 presents the impact of the Rayleigh number on streamline, temperature, and concentration contours inside a wavy baffled enclosure. The ascent of hot fluid from the heated bottom wall is restricted by the T-shaped fin, leading to complex multicellular flow patterns near the bottom surface (Fig. 12a). Furthermore, two weak secondary eddies are found in the vicinity of the upper portion of the baffle, indicating localized recirculation zones. At lower Ra, the flow circulations are notably weak due to reduced buoyancy effects. As Ra rises, the thermal buoyancy forces become more dominant, leading to a notable improvement in fluid motion. This results in the development of stronger eddies and more vigorous convective circulation within the cavity. Fig. 12b illustrates the isotherm patterns, revealing the intricate thermal behavior inside the cavity. Heated fluid initially rises but cools as it approaches the sidewalls, subsequently descending along these cooler boundaries. The adiabatic nature of the top wall alters this flow path, redirecting the motion and contributing to the accumulation of tightly spaced isotherms near the bottom region. This clustering highlights regions of intense thermal gradients, especially adjacent to the heated lower wall, where the large temperature differential enhances buoyancy-driven convection. The T-shaped fin significantly alters the thermal field by obstructing and redirecting heat flow, resulting in complex isotherm patterns and localized thermal gradients. It disrupts the direct upward movement of hot fluid, promoting lateral heat spreading and improved thermal mixing. At higher Rayleigh numbers, the fin

improves boundary layer thickening and uniform temperature distribution by interfering with buoyancy-driven flow. Overall, the fin plays a key role in optimizing heat transfer through its interaction with thermal gradients and convective motion. In Fig. 12c, the solutal lines depict solute dispersion inside the enclosure at $Le = 5$, $Rd = 1$, $Da = 10^{-3}$, and $Ha = 10$, highlighting detailed species transport dynamics. Their higher density compared to the energy contours indicates a higher rate of species transfer than thermal diffusion. We observe that as Ra increases from 10^4 to 10^6, the concentration distribution changes noticeably. The movement of fluid is stronger due to natural convection as the Rayleigh number increases. This motion helps to expand nanoparticles better.

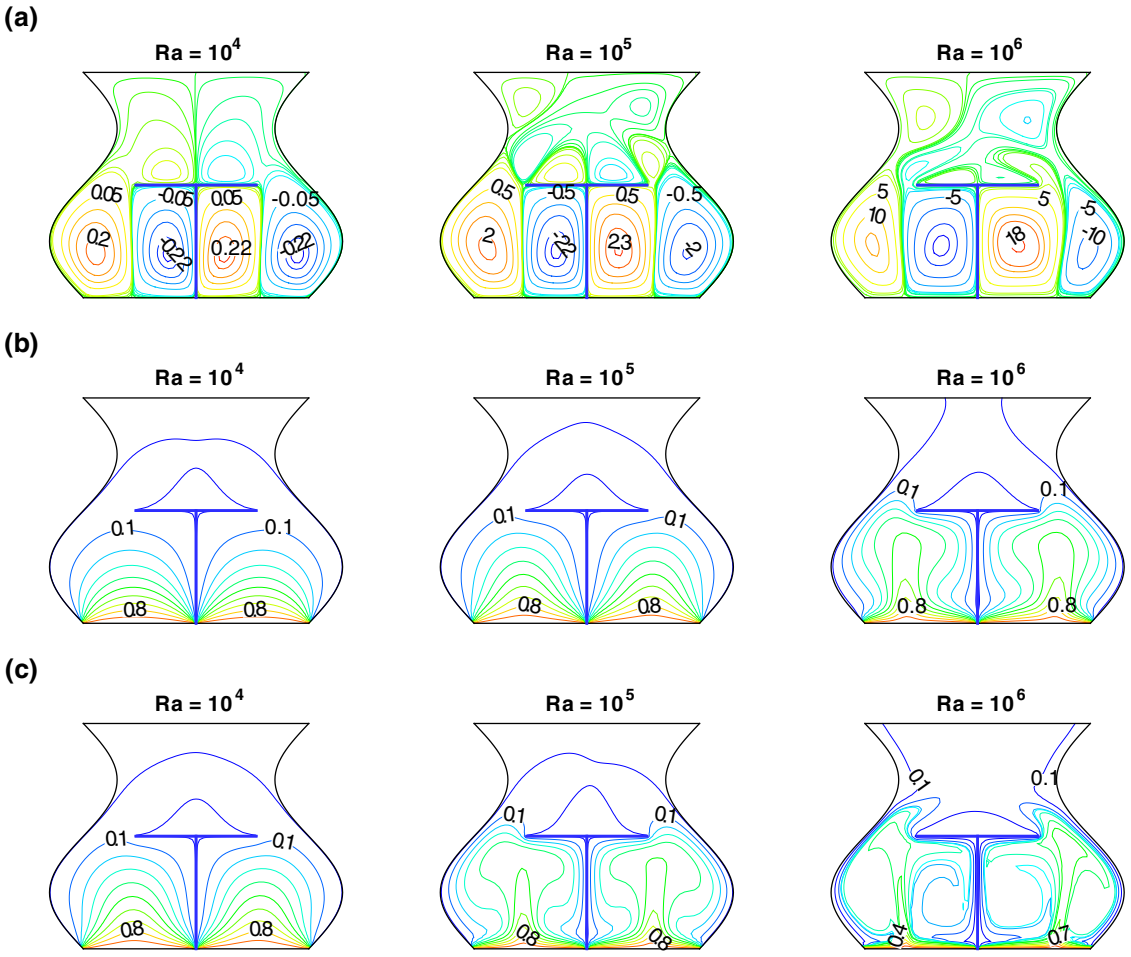

Figure 12: The effect of the Rayleigh number on (**a**) flow distribution, (**b**) isotherms, and (**c**) iso-solutal lines at $Le = 5$, $Rd = 1$, $Da = 10^{-3}$, $Ha = 10$.

Fig. 13a displays the influence of Le on the streamline contours. Physically, it determines the relative thickness of the thermal and concentration boundary layers in thermosolutal convection. The increasing hot fluid is obstructed, and the obstacle is redirected, near the obstacle, various small circular flows are developing. This exchange creates four main circulating regions and some weaker vortices inside the pot-shaped cavity. As the hot fluid flows downward through the cool side walls, the baffle slows part of its upward flow, leading to more circular flows appearing in the system. The flow distribution is basically changed in terms of the pattern as the Lewis number. Fig. 13b displays how thermal expansion occurs within the pot-shaped container. The temperature contours are very close to each other near the hot horizontal wall (bottom

wall), which means there is strong thermal transport in that region. When the Lewis number increases, there is not much temperature change. Fig. 13c observed that the iso-concentration contours are significantly changed as the values of Le. It is also observed that for higher values of Le, the temperature boundary layer becomes thicker than the mass boundary layer. Therefore, the thermal resistance is lower than the species resistance, and hence the mass transport is higher than the heat transport.

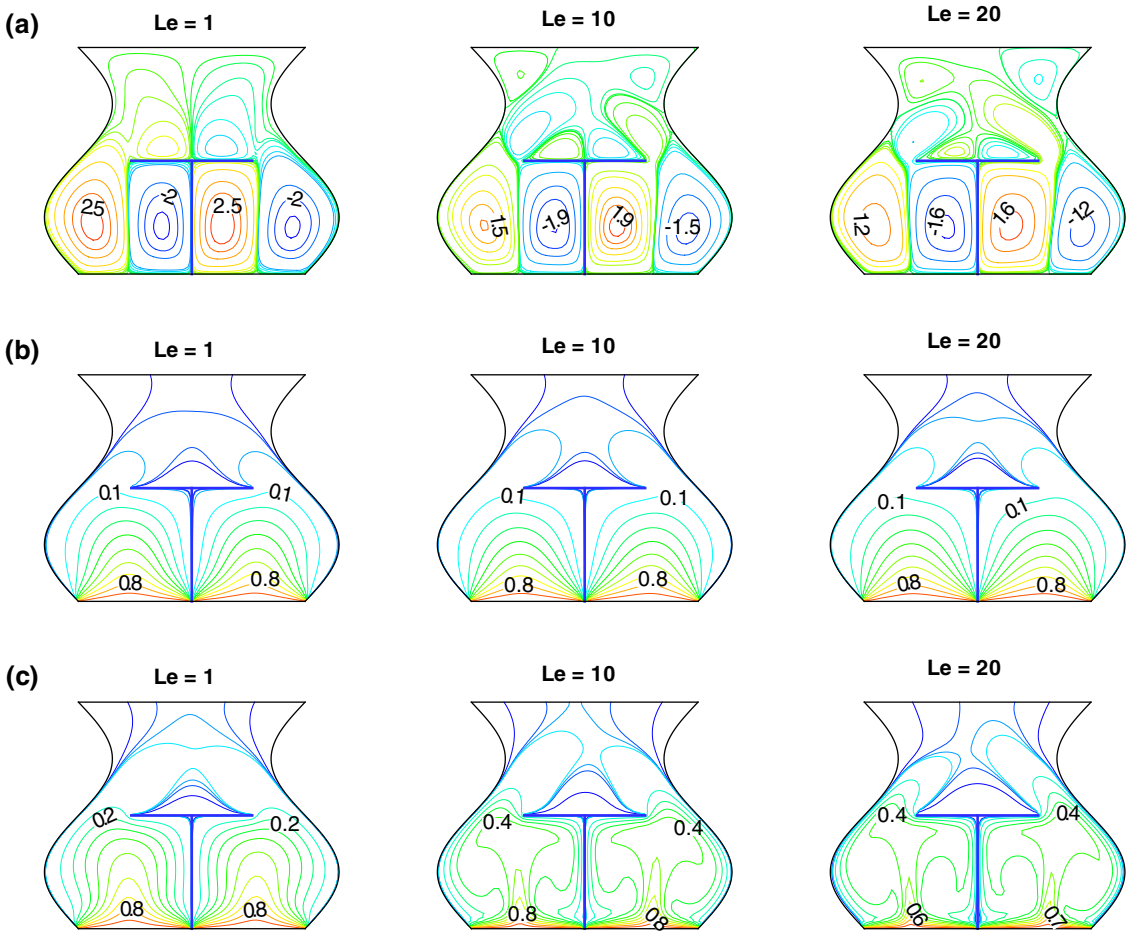

Figure 13: The effect of Lewis number on (**a**) flow distribution, (**b**) isotherms, and (**c**) iso-solutal at $Da = 10^{-3}$, $Ha = 15$, $Rd = 1$, $Ra = 10^5$.

Fig. 14a shows the influence of the Darcy number (Da) on the streamline in a cold T-shaped baffle inside the wavy cavity. The improving hot fluid is obstructed, and the obstacle is redirected, near the obstacle, various small circular flows develop. As Da increases from 10^{-5} to 10^{-3}, there is a change in the flow distribution. Fig. 14b shows how thermal expansion occurs within the cavity. When Da increases, there is no change in temperature. Fig. 14c displays how the concentration distribution occurs inside the container. When Da increases from 10^{-5} to 10^{-4}, there is no change in the concentration distribution. However, increasing Da from 10^{-4} to 10^{-3}, there are huge changes in the concentration distribution.

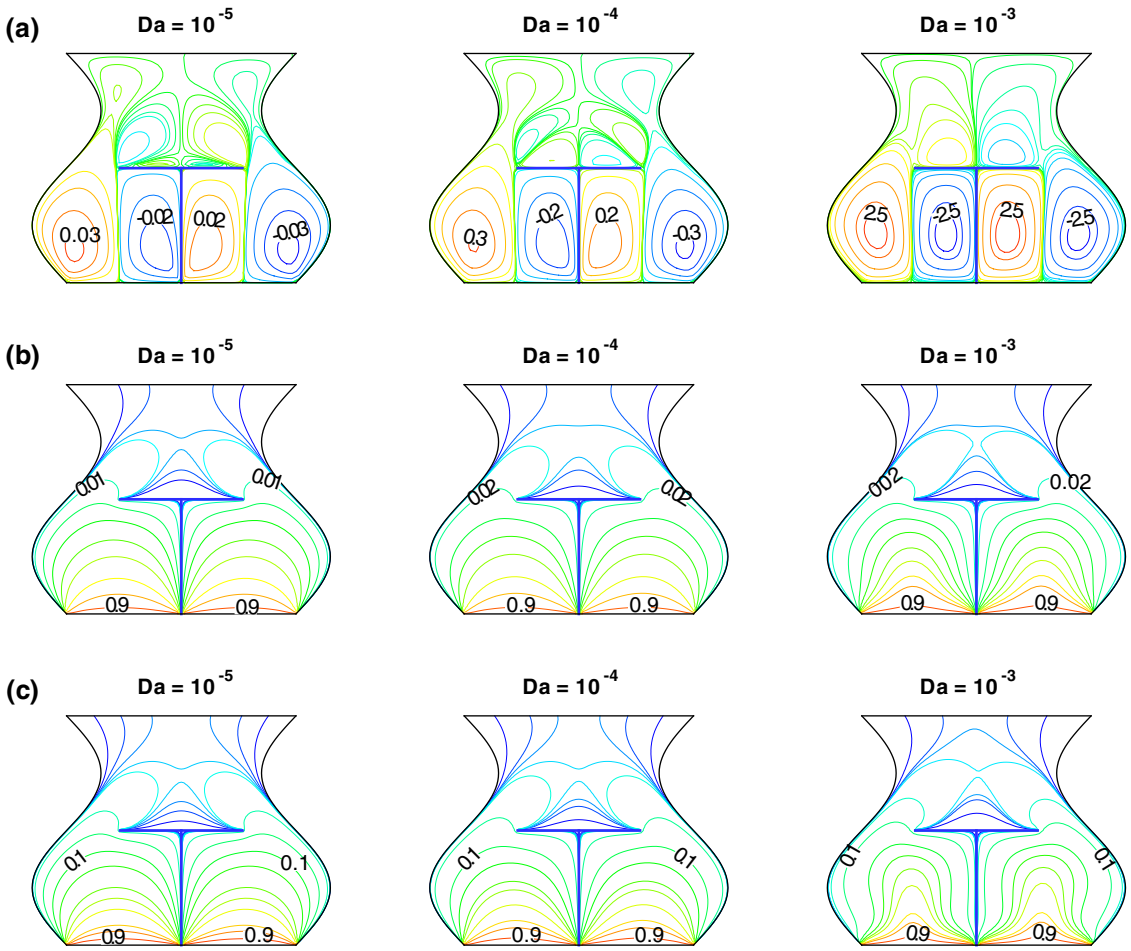

Figure 14: The effect of Darcy number on (**a**) flow distribution, (**b**) isotherms, and (**c**) iso-solutal at Le = 1, Ha = 10, Rd = 1, Ra = 10^5.

7.1 Thermosolual Activity and Entropy Production

This section presents a detailed discussion of the thermosolutal behavior and entropy generation characteristics of the system under the influence of different controlling parameters.

Fig. 15 illustrates the variation of Nu_{avg} and Sh_{avg} with different Rayleigh numbers and Casson fluid parameters. An upward trend is observed in both quantities, signifying improved heat and mass transport as these governing parameters increase. These observations indicate the effect of Ra on the thermal and species transfer characteristics inside the wavy enclosure. The intensity of buoyancy-driven flow is quantified by Ra, indicating stronger convection currents for higher values of Ra. When Ra increases, viscous forces become less influential than buoyancy-driven forces, leading to enhanced fluid movement and more effective thermal and species transport. The significant increases in Nu_{avg} and Sh_{avg} with increasing Ra highlight the transition from a conduction-dominated to a convection-dominated regime. For fixed γ, when Ra rises from 10^4 to 10^6, then both Nu_{avg} and Sh_{avg} increase by 16.99% and 135.54%, respectively. For Ra=10^6, Nu_{avg} and Sh_{avg} both increase by 30.20% and 91.21%, respectively, as γ increases from 0.1 to 10. In addition, the optimum values of Nu_{avg} and Sh_{avg} are observed in Ra =10^6 and γ = 10 with values 39.121 and 44.277, respectively.

The total entropy generation increases as Ra increases, due to stronger buoyancy-driven convection that improves thermal gradients and irreversibilities. In contrast, the Bejan number deteriorates because energy

transfer irreversibility dominates over fluid friction irreversibility at higher Rayleigh numbers (see Table 12). For fixed Ra = 10^6, the total entropy generation decreases 25.208% by increasing γ from 0.1 to 10, while the Bejan number increases by 86.666%. For fixed γ, the total entropy generation increases by 6204.930% when Ra improves from 10^4 to 10^6, while the Bejan number decreases by 97.168%.

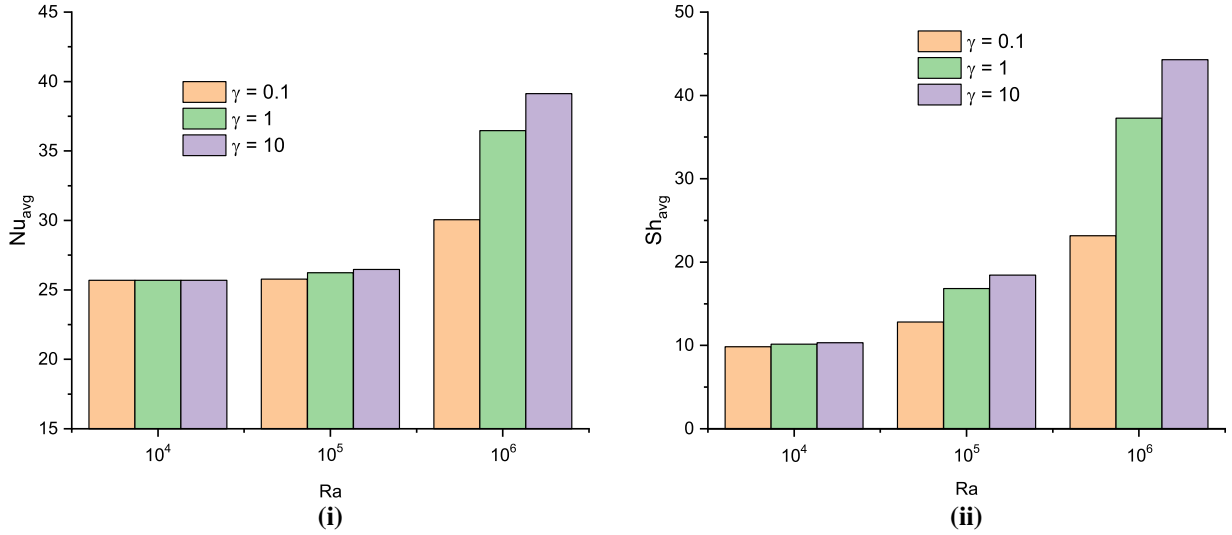

Figure 15: Effect of Rayleigh number (Ra) and Casson fluid parameters on (**i**) average Nusselt number (Nu_{avg}) and (**ii**) Sherwood number (Sh_{avg}) for $Le = 5$, $Rd = 1$, $Da = 10^{-3}$, $Ha = 10$.

Table 12: Total entropy generation (E_T) and Bejan number (Be) for different values of Rayleigh number and Casson fluid parameter.

Ra	E_T			Be		
	$\gamma = 0.1$	$\gamma = 1$	$\gamma = 10$	$\gamma = 0.1$	$\gamma = 1$	$\gamma = 10$
10^4	23.510	23.743	23.793	0.992	0.988	0.989
10^5	53.731	56.626	52.335	0.461	0.476	0.532
10^6	2005.760	1749.630	1500.132	0.015	0.022	0.028

Fig. 16 presents the effects of different Le and γ on Nu_{avg} and Sh_{avg}. These numbers improve as γ increases. When Le increases, the mass diffusivity decreases relative to the thermal diffusivity. This reduces species diffusion in the bulk, steepens concentration gradients near the walls, and increases Sh_{avg}. At the same time, the weakened solutal buoyancy contribution slightly suppresses convective strength, leading to a reduction in Nu_{avg}. For a particular value γ, Nu_{avg} decreases as Le increases, while Sh_{avg} increases. Nu_{avg} and Sh_{avg} increase by 1.406% and 69.31% respectively, as increasing value of γ from 0.1 to 10. For a particular value of γ, Nu_{avg} decreases by 2.05% as Le increases from 1 to 20, while Sh_{avg} increases 120.49%. In Fig. 17, we have demonstrated E_T and Be for different Le and for different γ. Entropy generation decreases with increasing Lewis number (Le) because higher Le implies weaker mass diffusivity relative to thermal diffusivity, which reduces concentration gradients and associated solutal irreversibility. However, the Bejan number increases with Le, indicating that heat-transfer irreversibility becomes more dominant compared to fluid-friction and mass-diffusion irreversibilities in E_T. For fixed γ, Be increases as the value of Le, while

E_T decreases. For a particular value of γ, E_T decreases by 27.19% as Le varies from 1 to 20, while the Bejan number increases by 77.37%.

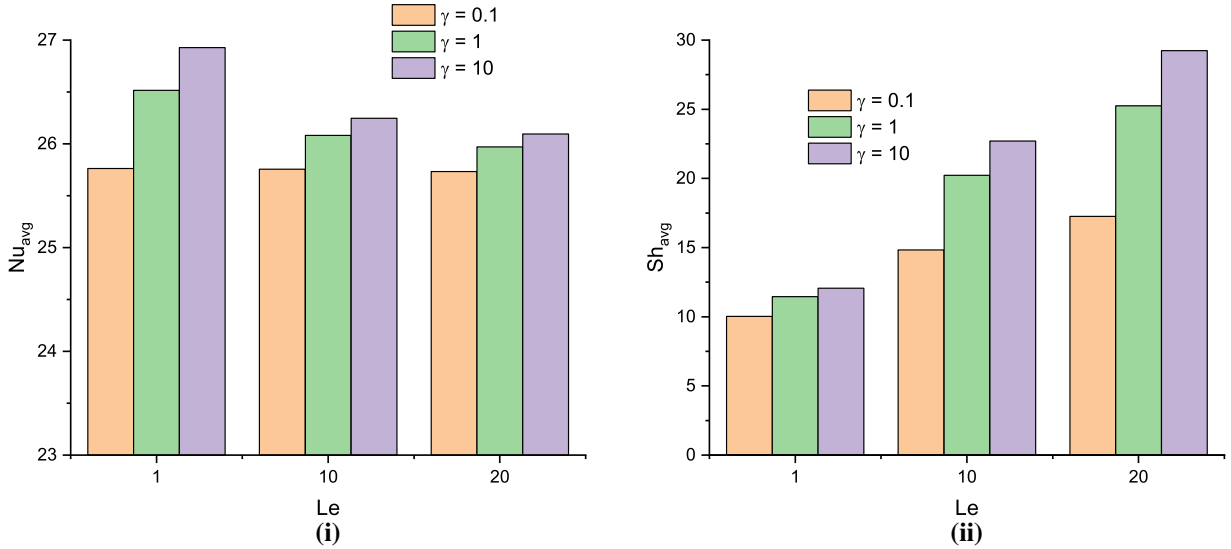

Figure 16: Effect of Lewis number and Casson fluid parameter on (**i**) average Nusselt number (Nu_{avg}) and (**ii**) Sherwood number (Sh_{avg}) at $Da = 10^{-3}$, $Ha = 15$, $Rd = 1$, $Ra = 10^5$.

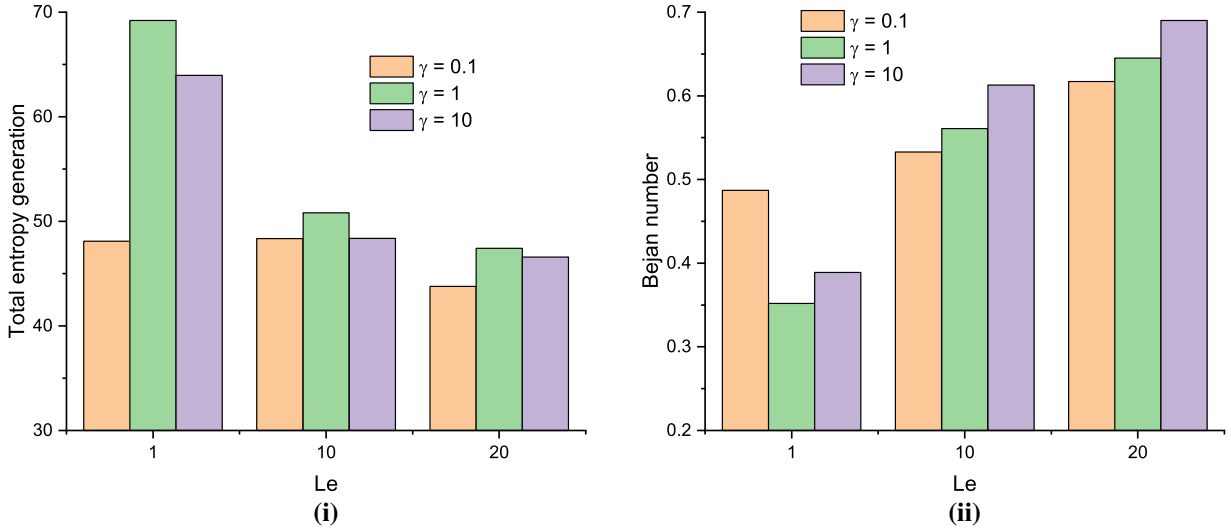

Figure 17: Effect of Lewis number and Casson fluid parameter on (**i**) Total entropy generation (E_T) and (**ii**) Bejan number (Be) at $Da = 10^{-3}$, $Ha = 15$, $Rd = 1$, $Ra = 10^5$.

Table 13 demonstrates the variation of Nu_{avg} and Sh_{avg} with different Darcy numbers and Casson fluid parameters. The permeability increased at higher Da, indicating fluid moves freely inside the enclosure. The enhancement of Nu_{avg} to improve fluid movement amplifies convection thermal transfer. Resulting in a higher Sh_{avg} permeability facilitates more effective mass transport. These observations indicate the balance between permeability and convection transport characteristics inside the wavy enclosure at higher Da. For fixed γ, both Nu_{avg} and Sh_{avg} increase 0.311% and 2.410%, respectively, by increasing Da from 10^{-5} to 10^{-3}. For fixed Darcy number 10^{-3}, both Nu_{avg} and Sh_{avg} increase by 4.557% and 20.426%, respectively,

to increase γ from 0.1 to 10. In Table 14 shows the change of E_T and Be with different Darcy numbers and Casson fluid parameters. As the Darcy number (Da) increases, entropy generation increases because a higher Da corresponds to greater permeability of the porous medium, allowing stronger fluid motion and larger velocity gradients, which intensify fluid-friction irreversibility. However, the Bejan number decreases with increasing Da, indicating that fluid-friction irreversibility becomes more dominant relative to heat-transfer irreversibility in the total entropy generation. The generation of entropy increases by 89.287% for $Da = 10^{-5}$ to 10^{-3}, while the Bejan number decreases by 47.001%.

Table 13: Variations of average Nusselt (Nu_{avg}) and Sherwood (Sh_{avg}) number for different values of Da and ϕ_{thnp} at for $Le = 1$, $Ha = 10$, $Rd = 1$, $Ra = 10^5$.

Da	Nu_{avg}			Sh_{avg}		
	$\gamma = 0.1$	$\gamma = 1$	$\gamma = 10$	$\gamma = 0.1$	$\gamma = 1$	$\gamma = 10$
10^{-5}	25.682	25.681	25.680	9.790	9.789	9.788
10^{-4}	25.682	25.683	25.681	9.803	9.818	9.821
10^{-3}	25.762	26.522	26.936	10.026	11.457	12.074

Table 14: Variations of total entropy generation (E_T) and Bejan number (Be) for different values of Da and γ at for $Le = 1$, $Ha = 10$, $Rd = 1$, $Ra = 10^5$.

Da	E_T			Be		
	$\gamma = 0.1$	$\gamma = 1$	$\gamma = 10$	$\gamma = 0.1$	$\gamma = 1$	$\gamma = 10$
10^{-5}	25.429	23.763	23.568	0.917	0.981	0.989
10^{-4}	35.491	27.605	25.995	0.657	0.844	0.897
10^{-3}	48.134	68.997	63.464	0.486	0.354	0.392

In Fig. 18, we have shown Nu_{avg} and Sh_{avg} for various values ϕ_{thnp} and for different γ. The inclusion of nanoparticles enhances heat transfer within the system due to improved effective thermal conductivity and intensified thermal diffusion, while it reduces solutal transfer because the presence of solid particles suppresses mass diffusivity and weakens concentration gradients. It is observed that for a fixed γ, Nu_{avg} increases with increasing values of ϕ_{thnp} while Sh_{avg} decreases. For fixed ϕ_{thnp}, Nu_{avg} and Sh_{avg} both increase with increasing values of γ. Nu_{avg} increases by 4.31% as the value of ϕ_{thnp} increases, while Sh_{avg} decreases by 0.95%. Both Nu_{avg} and Sh_{avg} increase by 31.41% and 45.95%, respectively, as enhancing the value of γ. In Fig. 19, we have shown E_T and Be for various values ϕ_{thnp} and for different γ. It is observed that for a fixed ϕ_{thnp}, E_T decreases as the values of γ increase, whereas Be increases. The addition of nanoparticles increases entropy generation due to stronger thermal gradients and higher viscous dissipation. However, the Bejan number decreases because the irreversibility of fluid friction becomes dominant over heat transfer irreversibility. For a fixed γ, these values are increase and decrease, respectively, as the volume of ϕ_{thnp}. Moreover, E_T and Be increase and decrease by 19.06% and 7.14%, respectively, as ϕ_{thnp} increases. In addition, E_T decreases by 33.58% as γ increases, while the Bejan number increases by 90%.

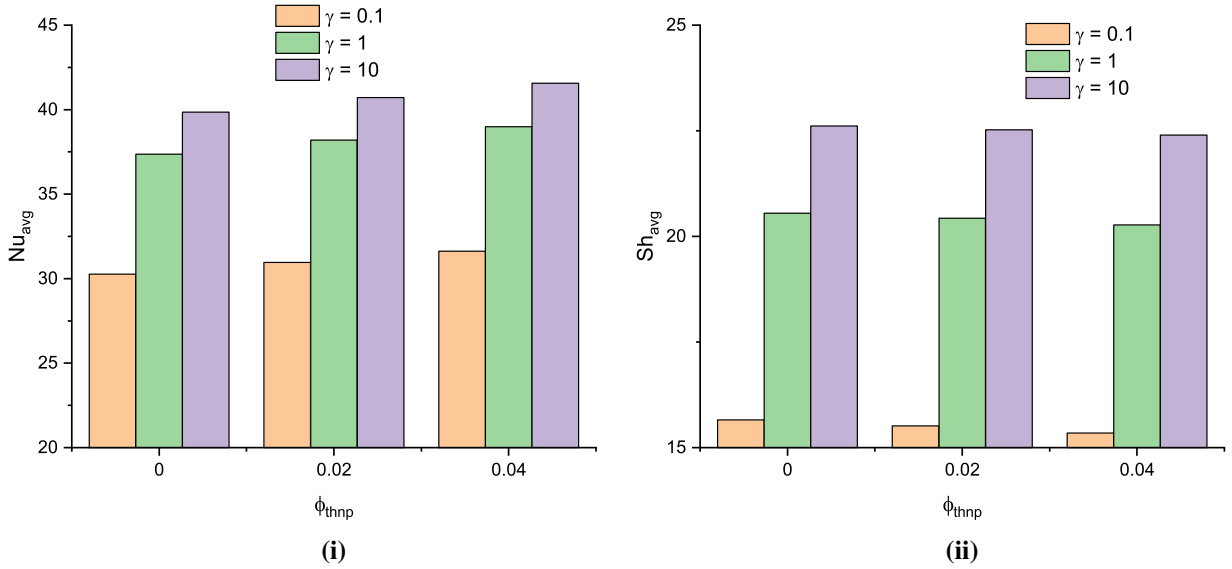

Figure 18: Effect of nanoparticles volume friction (ϕ_{thnf}) and Casson fluid parameter (γ) on (**i**) average Nusselt number (Nu_{avg}) and (**ii**) Shewrood number (Sh_{avg}) for $Le = 1$, $Da = 10^{-3}$, $Ha = 20$, $Rd = 1$, $Ra = 10^6$.

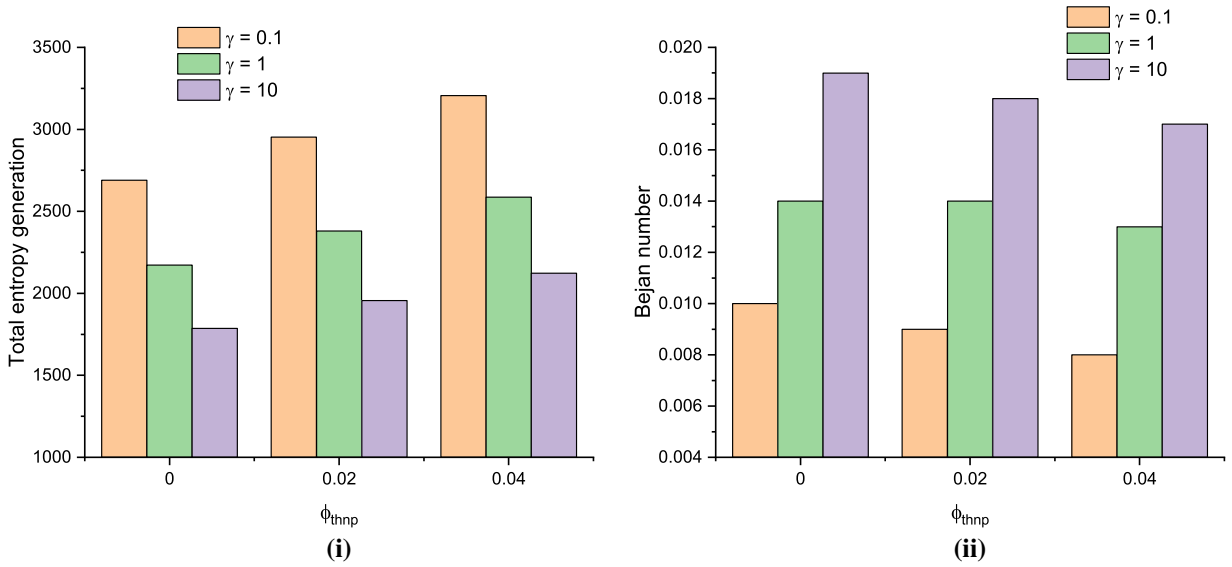

Figure 19: Effect of nanoparticles volume friction (ϕ_{thnf}) and Casson fluid parameter (γ) on (**i**) total entropy generation (E_T) and (**ii**) Bejan number (Be) for $Le = 1$, $Da = 10^{-3}$, $Ha = 20$, $Rd = 1$, $Ra = 10^6$.

In Fig. 20, we have shown Nu_{avg} and Sh_{avg} for various values Ha and for different γ. Higher values of Ha enhance the Lorentz force, which suppresses fluid motion and weakens convective transport, thereby reducing the Nusselt and Sherwood numbers. We find that increasing γ improves both quantities for a fixed Ha. Conversely, for a fixed γ, increasing Ha reduces both quantities. Nu_{avg} and Sh_{avg} increase by 2.49% and 13.36%, respectively, for γ value increases from 0.1 to 10. In addition, these numbers also decrease by 2.08% and 6.44% as Ha varies from 0 to 100. From Fig. 21, we have shown E_T and Be for different values of Ha and γ. For fixed γ, E_T boosts as Ha increases. For fixed $\gamma = 0.1$, the Bejan number increases when improving Ha. For $\gamma \geq 1$, Be decreases as Ha rises. E_T and Be decrease and increase by 4.86% and 4.93%, respectively, for

γ = 0.1, while the entropy generation increased by 9.21% for γ = 1, 29.05% for γ = 10, and the Bejan number decreased by 10.14% for γ = 1, 24.55% for γ = 10 as the value of Ha increases. In addition, E_T increases by 77.61% as γ increases, while the Bejan number decreases by 41.56%.

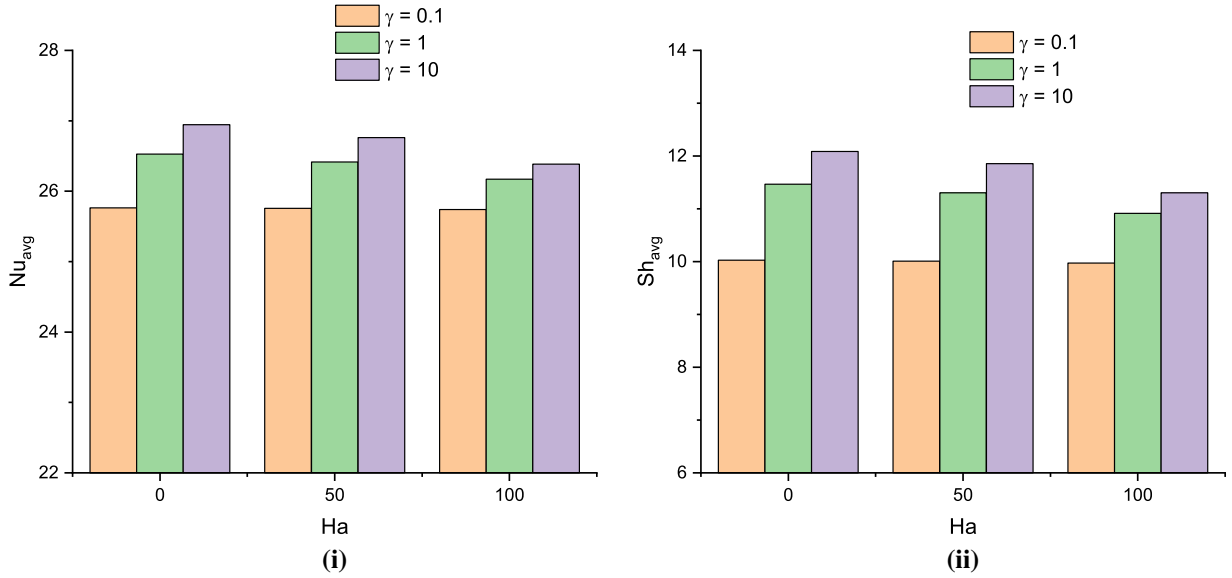

Figure 20: Effect of Hartmann number (Ha) and Casson fluid parameter (γ) on (**i**) mean Nusselt number (Nu_{avg}) and (**ii**) Shewrood number (Sh_{avg}) for various values for Le = 1, $Da = 10^{-3}$, Rd = 1, $Ra = 10^5$.

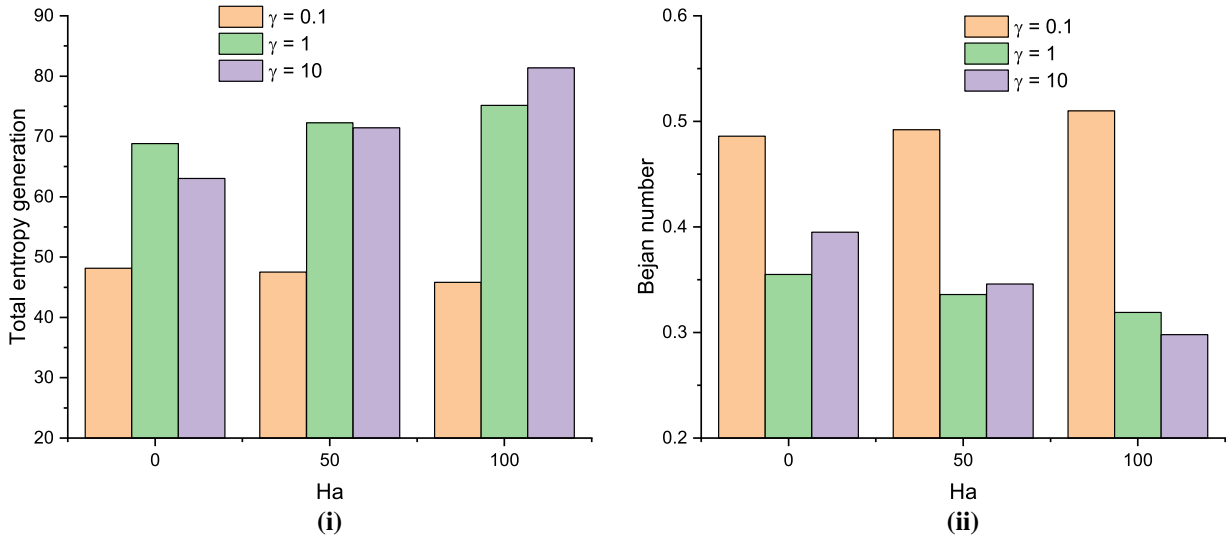

Figure 21: Effect of Hartmann number (Ha) and Casson fluid parameter (γ) on (**i**) Total entropy generation (E_T) and (**ii**) Bejan number (Be) for Le = 1, $Da = 10^{-3}$, Rd = 1, $Ra = 10^5$.

In Fig. 22, we have shown Nu_{avg} and Sh_{avg} for various values Rd and for different γ. For a fixed Rd, these values improve as γ increases. For a fixed γ, Nu_{avg} increases as Rd increases, while Sh_{avg} decreases. With an improvement in the radiation parameter, Nu_{avg} has increased by 216.71% and Sh_{avg} has decreased by 0.24%. With an increase in γ, Nu_{avg} has increased by 0.33% and Sh_{avg} by 17.51%. In Fig. 23, we have observed these numbers for different values and for various γ. For a particular value γ, E_T diminishes with

an increasing value of Rd while the Bejan number boosts. As Rd increases, entropy generation is reduced by 13.43%, while the Bejan number exhibits an increase of 12.59%.

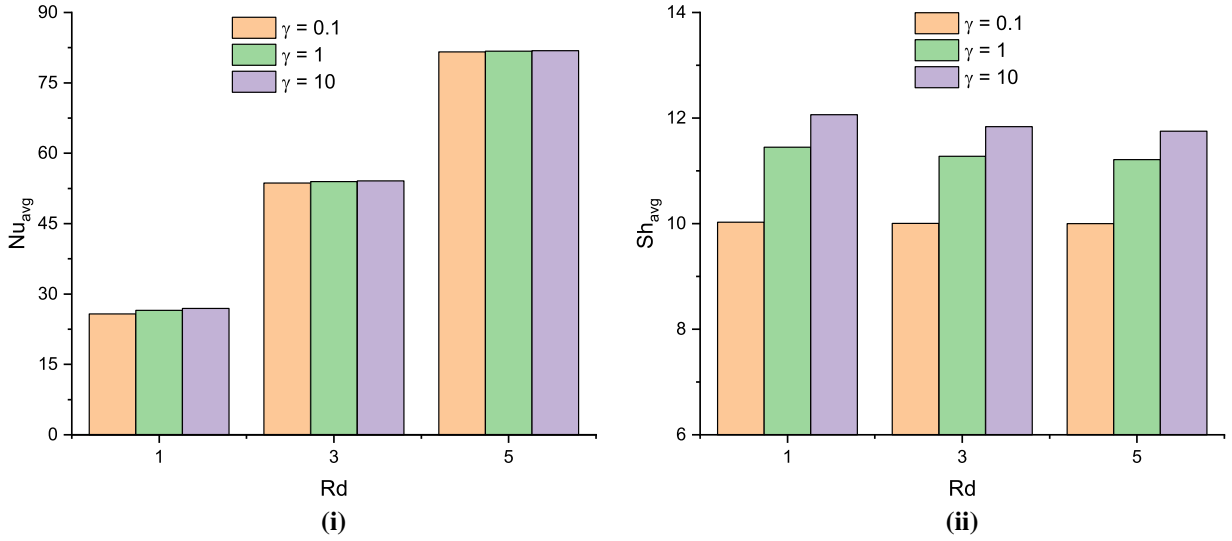

Figure 22: Effect of radiation parameter (Rd) and Casson fluid parameter (γ) on (**i**) average Nusselt number (Nu_{avg}) and (**ii**) average Sherwood number (Sh_{avg}) for $Le = 1$, $Ha = 15$, $Da = 10^{-3}$, $Ra = 10^5$.

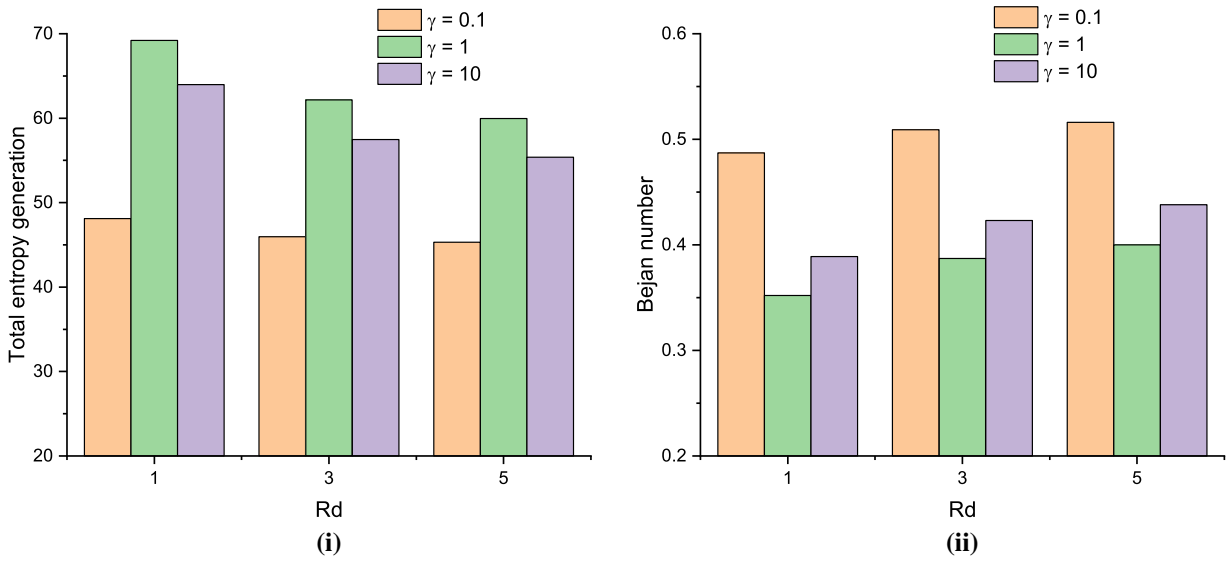

Figure 23: Effect of radiation parameter (Rd) and Casson fluid parameter (γ) on (**i**) Total entropy generation (E_T) and (**ii**) Bejan number (Be) for $Le = 1$, $Ha = 15$, $Da = 10^{-3}$, $Ra = 10^5$.

Entropy generation enhances with growing Ra and Da due to intensified buoyancy forces and higher porous medium permeability, which strengthen fluid circulation, thin boundary layers, and amplify velocity and thermal gradients, thereby enhancing both thermal and viscous irreversibilities. Similarly, the inclusion of nanoparticles and a stronger magnetic field further upgrade entropy production through augmented thermal gradients, Lorentz force-induced flow resistance, and increased viscous dissipation. In contrast, entropy generation reduces with rising Le because diminished solutal diffusivity weakens concentration gradients

and associated solutal irreversibility. Regarding the Bejan number, it dwindles with increasing Ra, Da, ϕ_{thnp}, and Ha, indicating the growing dominance of fluid-friction irreversibility, whereas it increases with Le, reflecting the relative predominance of energy transport irreversibility in the overall entropy generation. The maximum value of the entropy generation is recorded at $Ra = 10^6$, $Da = 10^{-3}$, $Le = 1$, $\phi_{thnp} = 0.04$, $Ha = 100$, $Rd = 1$, whereas the optimum Bejan number is attained at $Ra = 10^4$, $Da = 10^{-5}$, $Le = 20$, $\phi_{thnp} = 0.00$, $Ha = 100$, $Rd = 5$.

The Casson fluid parameter (γ) represents the relative effect of the yield stress on the fluid behavior. Low γ indicates a strong yield stress and higher hydrodynamic resistance, high γ reduces the effects of yield stress and lowers the apparent viscosity, making the fluid more Newtonian. For fixed parameters (Ra, Le, ϕ, Ha, and Rd), increasing γ reduces the yield stress and apparent viscosity, leading to stronger convection and free fluid flow. This thins the thermal and concentration boundary layers, leading to higher thermal and mass transport, thus Nu_{avg} and Sh_{avg} increase (Figs. 15, 16, 18, 20 and 22). As shown in Fig. 19, for fixed ϕ, increasing γ reduces yield strength and apparent viscosity. This reduces viscous (frictional) entropy generation, thereby decreasing E_T. Concurrently, thermal irreversibility becomes relatively increasingly dominant, so Be increases.

8 Conclusions

In this study, we carried out a numerical simulation of thermosolutal convection of a radiative Casson-based ternary aqueous nanofluid in a baffled porous cabinet. The enclosure is packed with a radiative $MWCNT$-Cu-Fe_3O_4/water ternary nanofluid, responsible for a complex interplay of entropy generation behaviors, solute, and thermal. We have explored the influences of key parameters, including the radiation number, Darcy number, Rayleigh number, Hartmann number, Lewis number, nanoparticle volume friction, Prandtl number, Casson fluid parameter, and buoyancy ratio. The analysis carried out has induced the following key results:

1. The improved thermosolutal efficiency and fluid circulation improved the transfer and flow mechanisms within the porous enclosure as a result of the existence of a cooled T-shaped baffle.
2. As Da increases, thermal transport, solute transport, and entropy production increase. This improvement intensifies convection thermal transport, more effective mass transport, and fluid friction irreversibility.
3. Increasing Ra from 10^4 to 10^6, also improves Nu_{avg} and Sh_{avg}. Resulted in an improvement of Nu_{avg} and Sh_{avg}, and thus improved the behavior of thermal and solute transport.
4. When the Lewis number increases from 0 to 20, resulting in a reduction in Nu_{avg}, the temperature gradient near the hot wall is reduced, while increasing Sh_{avg} and improving the transport of solutes when an element spreads slowly, the concentration gradient near the wall increases.
5. When Ra increases, buoyancy-driven forces become more influential than viscous forces, resulting in enhanced fluid movement and more effective energy and mass transfer.
6. Increasing Ha from 0 to 100, resulting in a decrease in both the Nu_{avg} and Sh_{avg} concentration and temperature gradients on the walls. Increasing Ha strengthens magnetic damping, which suppresses fluid movement and increases E_T due to higher magnetic and frictional irreversibilities. The Bejan number Be decreases as thermal irreversibility becomes less dominant. At $Ha = 0$, weak magnetic effects allow stronger convection, giving a higher Be.
7. When the radiation parameter (Rd) is such that Nu_{avg} increases, while Sh_{avg} decreases, indicating stronger thermal transport and less solutal diffusion. Increasing Rd improves radiative thermal transport, thus smoothing temperature profiles and reducing the total entropy generation (E_T). The Bejan number (Be) increases as thermal irreversibility becomes relatively more dominant.

The present findings offer practical guidance for the design of advanced thermal systems involving porous media and non-Newtonian nanofluids. The ability to modulate convection through magnetic control provides a viable strategy for stabilizing heat transfer in electronic cooling devices and compact heat exchangers. Although stronger buoyancy enhances thermal and solutal transport, it also increases entropy generation, indicating that optimal system performance requires balancing heat transfer augmentation with thermodynamic efficiency. The use of Casson ternary nanofluids can significantly improve effective thermal conductivity in solar collectors, thermal energy storage units, and process heat systems, but nanoparticle loading must be optimized to limit irreversibility. Furthermore, permeability tuning and strategic baffle placement offer additional design parameters for controlling flow structure and minimizing energy losses in porous reactors, geothermal installations, and filtration-based thermal systems.

Acknowledgement: This work was supported by the DST-FIST, Govt of India (File No.: SR/FST/MS-I/2022/123). The first author (Sarna Soren) is also grateful to UGC for her financial assistance UGC-JRF (D.O. No. 24D/03/01131). The authors also extend their appreciation for the support received from Universiti Kebangsaan Malaysia.

Funding Statement: The authors would like to express their appreciation for the support provided by Universiti Kebangsaan Malaysia through grant number GP-K017380.

Author Contributions: Sarna Soren: conceptualization, methodology, investigation, formal analysis, writing—original draft. Samrat Hansda: investigation, visualization, validation, writing—original draft. Umair Khan: conceptualization, writing—review & editing. Anuar Ishak: supervision, writing—review & editing. Ahmed Kadhim Hussein: data curation, visualization, investigation, methodology, writing—original draft. Md Mamun Molla: conceptualization, methodology, investigation, supervision, writing—review & editing. All authors reviewed and approved the final version of the manuscript.

Availability of Data and Materials: The data that support the findings of this study are available from the corresponding author, [Samrat Hansda], upon reasonable request.

Ethics Approval: Not applicable.

Conflicts of Interest: The authors declare no conflicts of interest.

Nomenclature

Pr	Prandtl number
A	Height of the cavity
Ra	Rayleigh number
Da	Darcy number
Ha	Hartmann number
B_0	Magnetic effect (Amp m^{-1})
Rd	Radiation parameter
Le	Lewis number, $Le = \frac{\alpha}{D}$
N	Buoyancy ratio parameter
Q	Volumetric heat source/sink coefficient
g	Gravitational acceleration (ms^{-2})
k	Thermal conductivity ($Wm^{-1}K^{-1}$)
p	Dimensional pressure (Nm^{-2})
P	Dimensionless pressure
T	Dimensionless temperature
k'_f	Permeability of the porous medium
C_p	Specific heat (J $Kg^{-1}K^{-1}$)

x, y	Dimensional Cartesian coordinates (m)
X, Y	Dimensionless Cartesian coordinates
u, v	Dimensional velocities in x, y directions respectively (ms^{-1})
U, V	Dimensionless velocities in X, Y directions respectively
ξ, η	Dimensionless coordinate in computational plane
Nu_{avg}	Average Nusselt number
Sh_{avg}	Average Sherwood number
$E_{l.h.t}$	Local entropy generation due to heat transfer
$E_{l.f.f}$	Local entropy generation due to fluid friction
$E_{l.m.f}$	Local entropy generation due to magnetic field
$E_{l.m.t}$	Local entropy generation due to mass transfer
E_T	Total entropy generation
Be	Bejan number
Greek letters	
α	Thermal diffusivity (m^2s^{-1})
β	Thermal expansion coefficient (K^{-1})
ϕ	Volume fraction of the hybrid nanoparticles
ρ	Hybrid nanofluid density(Kg m^{-3})
ν	Kinematic viscosity (m^2s^{-1})
μ	Dynamic viscosity (Pa s)
ψ	Stream function
ζ	Vorticity
σ	Electrical conductivity (μ S cm^{-1})
θ	Dimensional temperature
γ	Casson fluid parameter
$\varphi_1, \varphi_2, \varphi_3$	Irreversibility coefficient ratio
Subscripts	
i, j	Cell faces
f	Fluid
nf	Nanofluid
hnf	Hybrid nanofluid
hnp	Hybrid nanoparticles
$thnf$	Ternary hybrid fluid
$thnp$	Ternary hybrid nanoparticles

References

1. Ye L, Zheng T, Wang X, Liang X, Liu C. Evaluating the heat transfer characteristics of mesh-fed slot cooling configuration: influence of slot height and pin-fin arrangement. Appl Therma Eng. 2025;271(5):126304. doi:10.1016/j.applthermaleng.2025.126304.
2. Tang K, Lin G, Huang K, Qiao T, Guo Y. Visualized flow boiling regime evolution and diverging flow paths enhancement in manifold microchannel heat sinks. Int J Heat Mass Transf. 2026;259:128334. doi:10.1016/j.ijheatmasstransfer.2026.128334.
3. Eshaghi S, Izadpanah F, Dogonchi AS, Chamkha AJ, Hamida MBB, Alhumade H. The optimum double diffusive natural convection heat transfer in h-shaped cavity with a baffle inside and a corrugated wall. Case Stud Therm Eng. 2021;28(11):101541. doi:10.1016/j.csite.2021.101541.
4. Hansda S, Chattopadhyay A, Pandit SK, Sheremet MA. Irreversibility analysis of magneto-thermogravitational convection of radiative hybrid nanofluid in a U-shaped curvilinear porous container with a T-shaped baffle. J Therm Anal Calorim. 2024;149(22):13375–96. doi:10.1007/s10973-024-13607-5.

5. Hansda S, Chattopadhyay A, Pandit SK. Thermosolutal and hydromagnetic performance of radiative hybrid nanofluid in a wavy porous enclosure with a plus-shaped baffle. J Mol Liq. 2024 15;404(1):124880. doi:10.1016/j.molliq.2024.124880.
6. Kouki M, Nayak M, Irshad K, Al Mesfer MK, Danish M, Pasha AA, et al. Analysis of thermosolutal buoyancy-driven suspension comprising nano-encapsulated phase change materials using finite element method and ANN-based MLP algorithm. J Taiwan Ins Chemic Eng. 2025;168(7):105912. doi:10.1016/j.jtice.2024.105912.
7. Alsedais N, Aly AM. Double-diffusive convection from an oscillating baffle embedded in an astroid-shaped cavity suspended by nano-encapsulated phage change materials: ISPH simulations. Waves Random Complex Media. 2024;34(5):4533–52. doi:10.1080/17455030.2021.1994168.
8. Ahmad S, Liu D, Waqas H, Munir S. Numerical simulation of magnetohydrodynamics double-diffusive natural convection in a cavity with non-uniform heated walls. Appl Therm Eng. 2024;253(17):123778. doi:10.1016/j.applthermaleng.2024.123778.
9. Jain S, Nishad S, Bhargava R. Numerical simulation on double diffusion natural convection of a power-law nanofluid within double wavy cavity. Phy Fluids. 2021;33(7):507. doi:10.1063/5.0057309.
10. Hansda S, Majhi D, Hussein AK, Al-Sharify ZT, Abdulameer SF. Magento-double diffusive natural convection in a partially heated wavy porous cavity filled with a radiative hybrid nanofluid. J Therm Anal Calor. 2025;150(13):10489–512. doi:10.1007/s10973-025-14398-z.
11. Parmar D, Rathish Kumar B, Krishna Murthy S. Numerical study of time-fractional double diffusive convective flow in a wavy porous cavity. In: Mathematical theory and simulation of scientific problems. Berlin/Heidelberg, Germany: Springer; 2025. p. 11–20.
12. Parmar D, Murthy SK, Kumar BR, Kumar S. Numerical simulation of fractional order double diffusive convective nanofluid flow in a wavy porous enclosure. Int J Heat Fluid Flow. 2025;112(10):109749. doi:10.1016/j.ijheatfluidflow.2025.109749.
13. Alomari MA, Al-Farhany K, Al-Salami QH, Alyousuf FQ, Ali I, Biswas N. Numerical analysis of double-diffusive free convection in a curvilinear cavity filled with nanofluid and triple fins attached to the hot walls. Eur Phys J Plus. 2024;139(2):149. doi:10.1140/epjp/s13360-024-04941-6.
14. Chuhan IS, Li J, Ahmed MS, Samuilik I, Aslam MA, Manan MA. Numerical investigation of double-diffusive convection in an irregular porous cavity subjected to inclined magnetic field using finite element method. Mathematics. 2024;12(6):808. doi:10.3390/math12060808.
15. Hansda S, Chattopadhyay A, Pandit SK. Optimizing thermosolutal and hydrothermal performance of radiative hybrid ferrofluid and entropy generation in a wavy porous enclosure. J Magn Magn Mater. 2024;592(10):171774. doi:10.1016/j.jmmm.2024.171774.
16. Irshad K, Pasha AA, Al Mesfer MK, Danish M, Nayak M, Chamkha AJ, et al. Hydrothermal behavior and entropy analysis of double-diffusive nano-encapsulated phase change materials in a porous wavy h-shaped cavity with baffles: effect of thermal parameters. J Energy Storage. 2023;72(3):108250. doi:10.1016/j.est.2023.108250.
17. Tayebi T, El-Sapa S, Karimi N, Dogonchi AS, Chamkha AJ, Galal AM. Double-diffusive natural convection with Soret/Dufour effects and energy optimization of nano-encapsulated phase change material in a novel form of a wavy-walled I-shaped domain. J Taiwan Inst Chemic Eng. 2023;148(2):104873. doi:10.1016/j.jtice.2023.104873.
18. Uddin M, Rasel S, Adewole JK, Al Kalbani KS. Finite element simulation on the convective double diffusive water-based copper oxide nanofluid flow in a square cavity having vertical wavy surfaces in presence of hydro-magnetic field. Res Eng. 2022;13(9):100364. doi:10.1016/j.rineng.2022.100364.
19. Aly AM, Raizah Z, El-Sapa S, Oztop HF, Abu-Hamdeh N. Thermal diffusion upon magnetic field convection of nano-enhanced phase change materials in a permeable wavy cavity with crescent-shaped partitions. Case Stud Therm Eng. 2022;31(2):101855. doi:10.1016/j.csite.2022.101855.
20. Omara A, Touiker M, Bourouis A. Thermosolutal natural convection in a partly porous cavity with sinusoidal wall heating and cooling. Int J Numer Methods Heat Fluid Flow. 2022;32(3):1115–44. doi:10.1108/HFF-01-2021-0062.
21. Mansour MA, Ahmed SE, Mohamed EF, Ismaeel AM. Heat generation effects on MHD double diffusive of TiO_2-cu/water hybrid nanofluids in a lid-driven wavy porous cavity using LTNE condition. Sci Iran. 2025;32(3). doi:10.24200/sci.2023.61512.7353.

22. Mansour M, Bakier M. Magnetohydrodynamic mixed convection of TiO_2–Cu/water between the double lid-driven cavity and a central heat source surrounding by a wavy tilted domain of porous medium under local thermal non-equilibrium. SN Appl Sci. 2023;5(2):51. doi:10.1007/s42452-022-05260-0.
23. Hansda S, Soren S. Entropy generation and thermosolutal convection in a radiative porous chamber filled with a Casson-based ternary hybrid nanofluid and a cold square obstacle. Phys Fluids. 2025;37(8):082058. doi:10.1063/5.0281788.
24. Shahzad H, Ain QU, Pasha AA, Irshad K, Shah IA, Ghaffari A, et al. Double-diffusive natural convection energy transfer in magnetically influenced Casson fluid flow in trapezoidal enclosure with fillets. Int Commu Heat Mass Transf. 2022;137(1):106236. doi:10.1016/j.icheatmasstransfer.2022.106236.
25. El Hamma M, Elattari L, Nouari S. Double diffusion mixed convection in a porous cylindrical cavity filled with a Casson nanofluid driven by a lid, taking into account the Soret and Dufour effects. J Heat Mass Transf Res. 2025;12(1):81–90. doi:10.17654/0973576324026.
26. Chattopadhyay A. Hydromagnetic thermosolutal transient forced convection of radiative ternary hybrid ferrofluid with Casson fluid in a channel with a cavity and cylindrical obstacle. Phys Fluids. 2025;37(4):043115. doi:10.1063/5.0270468.
27. Alomari MA, Hassan AM, Alajmi A, Salho AK, Sadeq AM, Alqurashi F, et al. Analysis of double-diffusive transport and entropy generation in a wavy cylindrical enclosure with inner heated core: effects of MHD and radiation on Casson Cu-H_2O nanofluid. Energy Sci Eng. 2025;13(6):2810–41. doi:10.1002/ese3.70069.
28. Salho AK, Hassan AM, Alajmi A, Alomari MA, Sadeq AM, Alqurashi F, et al. Thermo-fluid dynamics of Cu-H_2O casson fluid in an H-shaped enclosure with Corrugated cylinders: a study of entropy generation, MHD, and radiation effects. Res Eng. 2025;25(6):104346. doi:10.1016/j.rineng.2025.104346.
29. Hussain S, Shoeibi S, Armaghani T. Impact of magnetic field and entropy generation of Casson fluid on double diffusive natural convection in staggered cavity. Int Commu Heat Mass Transf. 2021;127:105520. doi:10.1016/j.icheatmasstransfer.2021.105520.
30. Aghighi M, Ammar A, Masoumi H. Double-diffusive natural convection of Casson fluids in an enclosure. Int J Mech Sci. 2022;236(1):107754. doi:10.1016/j.ijmecsci.2022.107754.
31. Rashid U, Shahzad H, Lu D, Wang X, Majeed AH. Non-Newtonian MHD double diffusive natural convection flow and heat transfer in a crown enclosure. Case Stud Therm Eng. 2023;41:102541. doi:10.1016/j.csite.2022.102541.
32. Shah IA, Bilal S, Noeiaghdam S, Fernandez-Gamiz U, Shahzad H. Thermosolutal natural convection energy transfer in magnetically influenced Casson fluid flow in hexagonal enclosure with fillets. Res Eng. 2022;15(1):100584. doi:10.1016/j.rineng.2022.100584.
33. Chuhan IS, Li J, Guo Z, Shahzad H, Yaqub M. Entropy optimization of MHD non-Newtonian fluid in a wavy enclosure with double diffusive natural convection. Numer Heat Transf Part A Appl. 2024;85(16):2703–23. doi:10.1080/10407782.2023.2228482.
34. Aneja M, Sharma S. Heat and mass transfer due to double-diffusion convection in a square porous enclosure occupied by Casson fluid. In: Advances in fluid mechanics and solid mechanics. Berlin/Heidelberg, Germany: Springer; 2020. p. 91–9.
35. Chuhan IS, Li J, Zhao H, Guo Z, Yaqub M, Aslam MA. Impact of inclined magnetic field of Casson fluid on double diffusive natural convection in a curvilinear enclosure. J Phys. 2023;2599(1):012018. doi:10.1088/1742-6596/2599/1/012018.
36. Hansda S, Chattopadhyay A, Pandit SK, Sheremet MA. Thermosolutal performance of a non-Newtonian Casson fluid in a curvilinear porous baffled chamber with irreversibility and various heating strategies. Phys Fluids. 2025;37(2):023104. doi:10.1063/5.0251126.
37. Kathyayani G, Venkata Ramudu G. Mhd double-diffusive convection of Casson fluid in a triangular enclosure with thermal radiation and chemical reactions. Multiscale Multidiscip Model Exper Des. 2025;8(6):1–20. doi:10.1007/s41939-025-00874-4.
38. Hansda S, Chattopadhyay A, Pandit SK, Sheremet MA. Thermodynamics second law analysis for thermosolutal convection of a ternary aqueous suspension within a novel shaped porous container under an influence of Lorentz force and local heater. J Mol Liq. 2025;428(8):127488. doi:10.1016/j.molliq.2025.127488.

39. Pandit SK, Chattopadhyay A. A robust higher order compact scheme for solving general second order partial differential equation with derivative source terms on nonuniform curvilinear meshes. Comput Math Appl. 2017;74(6):1414–34. doi:10.1016/j.camwa.2017.06.031.
40. Pandit SK, Kalita JC, Dalal D. A fourth-order accurate compact scheme for the solution of steady Navier–Stokes equations on non-uniform grids. Comput Fluids. 2008;37(2):121–34. doi:10.1016/j.compfluid.2007.04.002.
41. Pandit SK, Chattopadhyay A, Oztop HF. A fourth order compact scheme for heat transfer problem in porous media. Comput Math Appl. 2016;71(3):805–32. doi:10.1016/j.camwa.2015.12.037.
42. Lele SK. Compact finite difference schemes with spectral-like resolution. J Computa Phys. 1992;103(1):16–42. doi:10.1016/0021-9991(92)90324-R.
43. van der Vorst HA. Bi-CGStab: a fast and smoothly converging variant of bi-CG for the solution of nonsymmetric linear systems. SIAM J Sci Stat Comput. 1992;13(2):631–44. doi:10.1137/0913035.
44. Al-Amiri AM, Khanafer KM, Pop I. Numerical simulation of combined thermal and mass transport in a square lid-driven cavity. Int J Therm Sci. 2007;46(7):662–71. doi:10.1016/j.ijthermalsci.2006.10.003.
45. Bettaibi S, Kuznik F, Sediki E. Hybrid LBM-MRT model coupled with finite difference method for double-diffusive mixed convection in rectangular enclosure with insulated moving lid. Phys A Stat Mech Its Appl. 2016;444(2):311–26. doi:10.1016/j.physa.2015.10.029.
46. Sompong P, Witayangkurn S. Simulation of natural convection in a complicated enclosure with two wavy vertical walls. Appl Math Sci. 2012;6(57–60):2833–42. doi:10.1155/2014/853231.
47. Pandit SK, Goswami KD, Chattopadhyay A, Öztop HF. On the analysis of magnetohydrodynamics and magnetic field-dependent viscosity effects on thermogravitational convection of hybrid nanofluid in an enclosure with curved walls. Phys Fluids. 2021;33(10):102010. doi:10.1063/5.0061451.
48. Ho C, Liu W, Chang Y, Lin C. Natural convection heat transfer of alumina-water nanofluid in vertical square enclosures: an experimental study. Int J Therm Sci. 2010;49(8):1345–53. doi:10.1016/j.ijthermalsci.2010.02.013.
49. Saghir MZ, Ahadi A, Mohamad A, Srinivasan S. Water aluminum oxide nanofluid benchmark model. Int J Therm Sci. 2016;109(9):148–58. doi:10.1016/j.ijthermalsci.2016.06.002.
50. Ma Y, Mohebbi R, Rashidi M, Yang Z, Sheremet MA. Numerical study of MHD nanofluid natural convection in a baffled U-shaped enclosure. Int J Heat Mass Transf. 2019;130(5):123–34. doi:10.1016/j.ijheatmasstransfer.2018.10.072.
51. Arefmanesh A, Najafi M, Musavi S. Buoyancy-driven fluid flow and heat transfer in a square cavity with a wavy baffle—meshless numerical analysis. Eng Anal Boundary Elements. 2013;37(2):366–82. doi:10.1016/j.enganabound.2012.11.004.
52. Ilis GG, Mobedi M, Sunden B. Effect of aspect ratio on entropy generation in a rectangular cavity with differentially heated vertical walls. Int Commun Heat Mass Transf. 2008;35(6):696–703. doi:10.1016/j.icheatmasstransfer.2008.02.002.